J. Fluid Mech. (2022), *vol*. 953, A31, doi:10.1017/jfm.2022.952

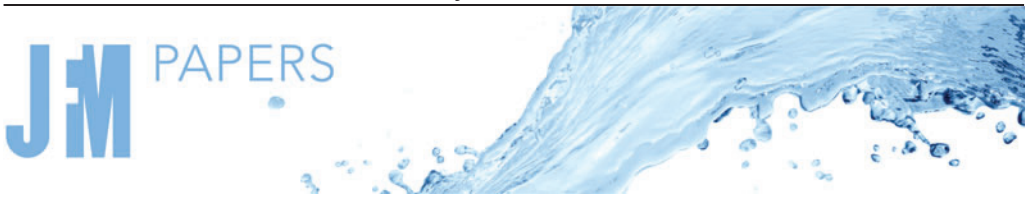

The interaction of longitudinal vortex pairs with a turbulent boundary layer

Andrew Mole[1],†**, Alex Skillen**[1] **and Alistair Revell**[1]

[1]Department of Mechanical, Aerospace and Civil Engineering (MACE), School of Engineering, University of Manchester, Manchester M13 9PL, UK

(Received 18 February 2022; revised 31 October 2022; accepted 6 November 2022)

In this study, we demonstrate an efficient approach to investigating the interaction of vortex pairs on a turbulent boundary layer. Our aim is to assess how vortex characteristics impact the downstream flow. Wall-modelled large eddy simulations are used together with an inlet defined by a Batchelor vortex model superimposed on a turbulent boundary layer profile, generated using synthetic turbulence and a precursor Reynolds-averaged Navier–Stokes calculation. This set-up allows for the efficient testing of multiple configurations whilst providing adequate resolution of outer boundary layer and the vortex–vortex interactions. After validating the methodology, we report a set of simulations for both co- and counter-rotating vortex pairs at different separations and asymmetric strengths. The separation distance between the vortices was found to have a significant effect upon the merging of the vortices. Asymmetric strength vortex pairs, analogous to vortex generators in yaw, demonstrate performance independent of flow direction for small angles. Detailed analysis of this flow provides insight into turbulence generation mechanisms and Reynolds stress anisotropy – valuable reference data for the development of lower-order models. Skin-friction enhancement is shown to be more effective for counter-rotating vortex pairs than co-rotating pairs of the same strength and spacing. Additionally, a wider spacing between the initial vortex positions results in a faster rise in the skin-friction coefficient.

Key words: turbulent boundary layers, rotating turbulence

1. Introduction

Turbulent boundary layers (TBLs) with embedded large-scale streamwise vortices represent an important class of three-dimensional wall-bounded flows due to their common occurrence. Vortices occur naturally in flow situations such as Görtler vortices on concave

† Email address for correspondence: andrew.mole@manchester.ac.uk

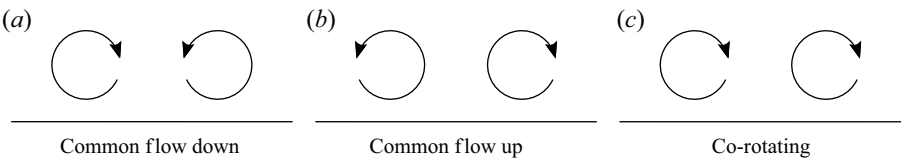

Figure 1. Diagram showing three configurations of vortex pairs and their naming.

plates (Görtler 1955) or horseshoe vortices at the base of a blunt object in contact with a boundary layer (Baker 1979, 1980). Streamwise vortices can also be intentionally introduced to boundary layers, via the use of vortex generators, often in order to delay or avoid separation under adverse pressure gradient conditions. This is done by exchanging momentum between the near-wall boundary layer and the free stream flow. This energises the near-wall flow, providing a delay in the onset of separation. Due to the large energy losses that can be caused by separation of a boundary layer, delaying its onset can considerably reduce the drag of the body. For this reason, vortex generators are prevalent in aerodynamic designs such as in aircraft (Bragg & Gregorek 1987), automotive (Aider, Beaudoin & Wesfreid 2010), motorsport (Pegrum 2007) and wind turbine blade (Gao *et al.* 2015) design, and have also found practical use in the enhancement of heat transfer (Torii & Yanagihara 1997).

Vortex generation devices generally introduce vortices in pairs, leading to three main flow configurations of interest: co-rotating, counter-rotating with a common flow upwards, and counter-rotating with a common flow downwards (Lögdberg, Fransson & Alfredsson 2009), as shown in figure 1. Due to the interaction with the wall, common flow upward vortex pairs tend to leave the boundary layer (Mehta & Bradshaw 1988), while common flow downward vortex pairs are held within the boundary layer for a longer period downstream of the generator (Pauley & Eaton 1988). The use of vortex generators in complex flow applications, for example those found on the wings or diffusers of both aircraft and land vehicles, can lead to uncertainty or variation in the yaw alignment of the vortex generators. This skewed flow to the vortex generators can lead to an imbalance in strength between the pair of vortices that are designed to be of equal strength. Assessing the interaction of unbalanced vortex pairs is important in order to understand both the performance and robustness of vortex generators in their application. The wide variance possible in the set-up and configuration of vortex generators makes it difficult to assess which variables are important for increasing the effectiveness of the vortices at delaying the onset of separation.

Early work on the effect of vortex generating devices by Taylor (1947) looked at rows of aerofoils mounted within a boundary layer. This was followed by a study by Spangenberg & Schubauerand (1960), who compared the effect of the addition of vortex generators to varying adverse pressure gradient boundary layers. They concluded that the increased mixing introduced by the vortex generators had an effect comparable to reducing the pressure gradient. Pearcy (1961) investigated different vortex pair configurations – common flow down, common flow up, and co-rotating vortices – and focused on the design of the vortex generators. The study also tracked the movement of the vortices produced by a common flow down vortex generator design, showing that the vortices initially dipped towards the wall before being held at a constant height within the boundary layer. The dynamics of a common flow up vortex pair was presented by Mehta & Bradshaw (1988), showing that the vortices were lifted out of the boundary layer before settling at a height of approximately twice the boundary layer thickness, above the wall. The boundary layer

thickness, denoted δ, is defined as the height above the surface at which the velocity has reached 99 % of the free stream velocity.

The evolution of both the mean velocity and the Reynolds stresses of a single vortex interacting with a turbulent boundary layer were investigated by Westphal, Pauley & Eaton (1987). This was extended by Pauley & Eaton (1988) to include pairs and arrays of longitudinal vortices embedded within a turbulent boundary layer. A range of blade angles and separation distances were investigated for the common flow down vortex pair case as well as presenting results for common flow up and co-rotating vortices. They found that the rate of spreading of the vorticity was increased by the presence of nearby vortices.

In their work on the design of vortex generator devices, Wendt (2001) investigated the initial circulation and peak vorticity generated from different geometries. Among other parameters, it was found that the strength of the vortex produced was proportional to the angle of the blade compared to the flow direction. A further optimisation study performed by Godard & Stanislas (2006) found that counter-rotating vortex pairs performed better than co-rotating pairs, indicated by a larger increase in the skin friction at the wall, and defined an optimal angle of the vortex generator to the incoming flow direction under the given conditions. The experimental work of Lögdberg *et al.* (2009) looked at different configurations of counter-rotating vortices and the effect that yaw had on the vortex development. They found that adjusting the yaw angle between 0° and 20° led to a linear increase in the strength of one vortex and a linear decrease in the other, with the total circulation remaining broadly constant. It was found that this also had an effect on the vortex paths with both vortices moving in the direction of the now stronger vortex, and the weaker vortex staying closer to the wall.

Early numerical studies, including those by Liandrat, Aupoix & Cousteix (1987), Sankaran & Russell (1990) and Kim & Patel (1994), employed a variety of Reynolds-averaged Navier–Stokes (RANS) models for the computation of longitudinal vortices embedded in a turbulent boundary layer. Mean flow field predictions were found, in general, to be quite reasonable around and away from the vortex core. Numerical predictions at the vortex core were less favourable when using standard linear eddy viscosity models, with axial velocity and vorticity both being significantly lower than expected. This was due to both excessive numerical diffusion and over-prediction of turbulence kinetic energy in this region. Guohua & Guanghua (1998), and more recently Spalart *et al.* (2015), applied a series of nonlinear eddy viscosity models to similar flows, the latter with a specific curvature correction term included to reduce the turbulence generation in the vortex core. While these modifications helped to improve predictions, they did not achieve sufficient reduction in the levels of turbulence at the core needed to ensure the persistence of the vortex. Second moment closure methods, based on modelling the transport of the Reynolds stress components individually, have been shown to improve the representation of the turbulence statistics, such as the study of wingtip vortices by Craft *et al.* (2006), and the application to three-dimensional boundary layer flows by Billard, Revell & Craft (2012). Esmaili & Piomelli (1992) and then Liu, Piomelli & Spalart (1996) used large eddy simulations (LES) to replicate the common flow down vortex pair case of Pauley & Eaton (1988). They reproduced the effect of the vortex generators by superimposing a Batchelor vortex pair over a recycled and rescaled turbulent boundary layer. They found that they were able to better match the mean velocity with a reduction in the peak streamwise vorticity matching far closer to that found in the experimental cases. They were also able to accurately match the turbulence statistics in the vicinity of the vortex core. Off-design conditions of vortex generators were also investigated by

Baldacchino *et al.* (2016) using a point vortex model. Whilst exploring the parameter space of asymmetric vortex pairs, they found that two regimes existed, defined as translating and orbital trajectories. However, this model did not include viscous diffusion or high Reynolds number effects.

While nonlinear RANS and stress-transport models bring improvement to the prediction of these flows, the use of scale-resolving methods is expected to be required to accurately predict the interaction of the vortices and the boundary layer. The practical compromise of hybrid RANS-LES (HRL) methods is therefore appealing, as demonstrated in their application to aerospace flows in various applied aerospace cases considered in Haase, Braza & Revell (2009). Of the various HRL approaches developed in the past two decades, one of the more promising candidates is embedded/zonal simulation, whereby a RANS model is used away from the region of interest, and LES are employed where improved accuracy is required. The two approaches can be bridged by the use of synthetic turbulence approximations (see e.g. Holgate *et al.* 2019, for a recent review). In the present work, we begin by demonstrating the capability of an efficient scale-resolving framework based on use of synthetic turbulence and wall-modelled LES. In this regard, we are motivated by the work of Liu *et al.* (1996) and seek to validate the present methodology with their work using rescaling methods. In doing so, we also compare our work to experimental data of flow in the wake of vortex generation devices, demonstrating that the present framework avoids the need to resolve directly the geometry of these devices. The framework is used in order to provide an accurate representation of the downstream interaction between the vortex pairs and the boundary layer, whilst remaining computationally efficient and flexible enough to explore configurations with varying vortex strength, positioning and rotation direction. Our second objective is to build on previous experimental and modelling work on embedded vortices in a zero pressure gradient (ZPG) turbulent boundary layer, to provide further physical insight using a combination of wall data, the impact on the mean boundary layer, and a detailed analysis of turbulence quantities. The resulting data and discussion will provide insight into the current performance and future improvement of both RANS and reduced-order models relevant for industrial development of vortex generators.

In the following, § 2 describes the numerical methods employed and the framework used to introduce vortices into the turbulent boundary layer. In § 3, the method is applied to a ZPG turbulent boundary layer with no vortices, before we present in § 4.1 our results validating the method with a common flow down vortex pair compared to experimental results. Further analysis of counter-rotating and co-rotating vortices is presented in § 4.2. The method is then extended to provide analysis of cases including skewed vortex generators and variation in separation distance in § 4.3, before conclusions are drawn in § 5.

2. Methodology

2.1. *Governing equations*

The present approach comprises a RANS computation of the full boundary layer domain used as a precursor calculation and a smaller LES domain situated within. This allows for the scale resolving LES to be used where it is required in predicting the interaction between the multiple vortices and the turbulent boundary layer, with the inlet conditions supplied from the precursor RANS calculation and a vortex model. Figure 2 shows the set-up of the two domains.

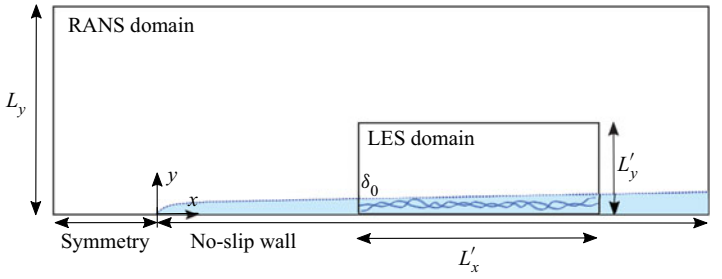

Figure 2. Diagram showing the set-up of the RANS domain and LES domain for the base case of a ZPG turbulent boundary layer.

In the LES region, the filtered Navier–Stokes equations are solved. These are given by

$$\frac{\partial \langle \boldsymbol{u}_i \rangle}{\partial \boldsymbol{x}_i} = 0, \quad \frac{\partial \langle \boldsymbol{u}_i \rangle}{\partial t} + \frac{\partial \langle \boldsymbol{u}_i \boldsymbol{u}_j \rangle}{\partial \boldsymbol{x}_j} = -\frac{1}{\rho} \frac{\partial \langle p \rangle}{\partial \boldsymbol{x}_i} + \nu \frac{\partial^2 \langle \boldsymbol{u}_i \rangle}{\partial \boldsymbol{x}_j^2}, \tag{2.1}$$

where the vector $\boldsymbol{x}_i$ comprises $x_1 = x$, $x_2 = y$ and $x_3 = z$, being the streamwise, wall-normal and spanwise directions, respectively. Correspondingly, $\boldsymbol{u}_i = (u, v, w)$ is the velocity vector field, with the subscript i denoting the direction. Also, p is the pressure field, ρ is the fluid density, and ν is the kinematic viscosity of the fluid. The angle brackets denote a filtering operation, and the turbulence stress terms $\langle \boldsymbol{u}_i \boldsymbol{u}_j \rangle$ comprise both the resolved term and the effect of the sub-grid scales, which are modelled using a sub-grid scale (SGS) model. When presenting results, an overbar represents time averaging, and a dash represents the remaining fluctuating part of the field.

In order to relax the grid requirements needed to complete wall-resolved LES (WRLES), a hybrid RANS-LES model was used. By using the improved delayed detached eddy simulation (IDDES) implementation of Shur *et al.* (2008) in the configuration designed for wall-modelled LES (WMLES), the grid spacing in the streamwise and spanwise directions can be increased considerably, since only the outer region of the turbulent boundary layer, $y/\delta > 0.1$, is treated with LES, while the inner region is handled with a RANS model. To appreciate the magnitude of this saving, Piomelli (2008) estimated that for $Re \approx 10^6$, the number of mesh cells required to resolve the inner region of the boundary layer, as required in WRLES, is around two orders of magnitude higher than the number of cells needed in the outer region. In this study, the Spalart–Allmaras one-equation RANS model is used to model turbulence quantities in the inner boundary layer, before switching rapidly to full LES away from the wall. The WMLES branch is designed to be activated in the presence of unsteady inflow conditions provided that the grid is sufficiently fine for resolving the dominant eddies found within a turbulent boundary layer. More details of the WMLES model can be found in Appendix A and in the paper of Shur *et al.* (2008).

The inlet boundary conditions to the LES domain are obtained from the RANS domain, for which the Spalart–Allmaras turbulence model is used, details of which can be found in the paper of Spalart & Allmaras (1992). The current work uses a formulation without the trip term or ft2 term implemented, and with a limiter on the modified vorticity term to prevent negative values. The Spalart–Allmaras turbulence model was chosen for the background RANS calculation as it is particularly well calibrated for use on boundary layer flows and follows the methodology applied in earlier studies using similar techniques on turbulent boundary layers (Mockett, Haase & Schwamborn 2017). In order

to transition effectively from the RANS-modelled description of the flow in the precursor calculation to the region of LES, turbulence fluctuations in the velocity field must be introduced as these are not present in the averaged flow field of the RANS calculation. The synthetic eddy method (SEM), first proposed by Jarrin *et al.* (2006), is an efficient method used to introduce fluctuations to the velocity field at the LES inlet that can be applied to inhomogeneous fields. The method superimposes a prescribed number of randomly positioned eddies onto the mean velocity field, which are then scaled to match the spatial estimate of turbulence provided from the RANS model. The resulting fluctuating velocity field contains turbulent structures that are coherent in both time and space, and exist over a range of scales. Further details of the method used in this investigation, including improvements to the original SEM, are presented in the work by Skillen, Revell & Craft (2016).

In this study, the finite volume code OpenFOAM-v1812 is used (Weller *et al.* 1999). For the LES, the coupled momentum and pressure equations are solved using the PISO algorithm with the time integration performed using a second-order backwards differencing, and spatial discretisation done using second-order schemes. For the precursor RANS calculation, the SIMPLE algorithm is used for the coupling of the momentum and pressure equations, with spatial discretisation performed using second-order schemes.

2.2. *Boundary conditions*

For the precursor two-dimensional RANS calculation, the domain is set up following the validation case of Rumsey, Smith & Huang (2009). The velocity inlet boundary condition is defined by a uniform Dirichlet condition $U_x = U_0 = 70\,\mathrm{m\,s^{-1}}$. The outlet and top velocity boundary conditions are zero-gradient Neumann conditions, while the lower boundary has an initial section of a symmetrical boundary condition followed by a no-slip wall, as shown in figure 2. The pressure inlet condition is zero-gradient Neumann, with the other pressure boundaries zero-value Dirichlet conditions. The turbulence quantity for the Spalart–Allmaras model at the inflow is set to be three times the kinematic viscosity, $\tilde{\nu} = 3\nu$, based on the recommendation by Spalart & Rumsey (2007).

For the LES domain, the SEM is used to define the inlet velocity, based on the information from the precursor RANS calculation. The turbulence quantities at the inflow are taken from the value of $\tilde{\nu}$ from the precursor RANS model multiplied by the blending functions f_B and f_{e1} given in Appendix A as (A2*a*,*b*) and (A4*a*,*b*). A no-slip condition is applied along the lower wall, whilst the outlet and top velocity boundary conditions are zero-gradient Neumann conditions, and the front and back boundaries are periodic in the lateral direction as vortex generators are often found in arrays and match the set-up used by Liu *et al.* (1996). The pressure inlet condition is zero-gradient Neumann with the top, wall and outlet pressure boundaries defined with zero-value Dirichlet conditions.

2.3. *Vortices*

The vortex generators themselves are not resolved in this study. Instead, a simple vortex model is used to represent their downstream impact on the mean velocity field. The model is then combined with both the RANS turbulent boundary layer profile and the synthetic turbulence fluctuations to provide the inlet condition for the LES domain. In this way, the LES domain can be considered to start immediately downstream of the vortex generator.

A velocity field is generated to model the inclusion of the vortex by using the Batchelor vortex model (Batchelor 1964). In order to model a vortex pair, two Batchelor vortices are introduced, and in order to enforce the non-permeable condition imposed by the solid wall, two additional mirror vortices are also included beneath the wall, as illustrated in figure 3, corresponding to each of the real vortices. The velocity fields of the individual vortices are created using a form of the Batchelor vortex equations that Velte, Hansen & Okulov (2009) found matched experimental results. The azimuthal velocity is defined by

$$V_\theta = \frac{qR}{r}\left[1 - \exp\left(-\frac{r^2}{R^2}\right)\right], \tag{2.2}$$

where q is the strength of the vortex, r is the distance away from the centre of the vortex, and R is a length scale corresponding to the radius of the vortex core. To model the streamwise velocity deficit introduced in real vortex generators by the delta-wing-shaped devices, a velocity component in the streamwise component is included, defined by

$$V_x = q_w \exp\left(-\ln(2)\,\frac{r^2}{R^2}\right), \tag{2.3}$$

where q_w is the strength of the wake, and the constant $\ln(2)$ is used to set the magnitude of V_x at the edge of the core to be half the maximum magnitude. Two vortices and their corresponding mirror vortices can then be defined with centres in the wall-normal direction $y = \pm H_v$, and in the spanwise direction at $z = \pm S_v/2$. In order to enforce the no-slip condition at the wall, the azimuthal velocity is reduced linearly from distance $y/\delta_0 = 0.1$, where δ_0 is the boundary layer height at the LES inlet location. The Batchelor vortex model presented provides an approximation of the vortices found in the wake of a vortex generator and makes the assumption that the vortices are rotationally symmetrical and do not contain a radial component. The effects of these assumptions are considered relatively minor compared to the contribution of the azimuthal velocity component. Only the effect of the vortices on the velocity field is considered here, and no additional turbulence is introduced beyond that from the boundary layer. This limitation of the approach is difficult to avoid as a model of the additional turbulence would depend strongly on the specific geometry of the vortex generators. In § 4.1, the resulting flow of this model is compared to that found experimentally in the wake of a pair of vortex generators by Pauley & Eaton (1988). The comparison suggests that the flow would not be particularly sensitive to additional turbulence contributions, with the interaction between the vortices and the boundary layer turbulence dominating the behaviour.

The strength (q) and radius (R) of the vortices can be defined independently in order to achieve a configuration that represents the vortices generated by a skewed vortex generator. As shown in figure 3, when the flow direction is skewed by angle α, the relative angles of the vortex generators are $\beta \pm \alpha$, where β is the designed angle of the vortex generator. It is then this relative angle that correlates to the strength of each vortex. In this study, the effects of varying vortex configurations are investigated by varying the relative signs of the vortices, with $q_1/q_2 = -1$ describing counter-rotating vortices, and $q_1/q_2 = 1$ co-rotating vortices. The separation distance (S_v) between the vortices for both counter-rotating and co-rotating vortex pairs, and the effect of varying the skew angle (α), are explored in § 4.3.

2.4. *Mesh*

The meshes used for the WMLES calculations are constructed according to best practice guidelines from a study of the same baseline case in the EU project 'Go4Hybrid'

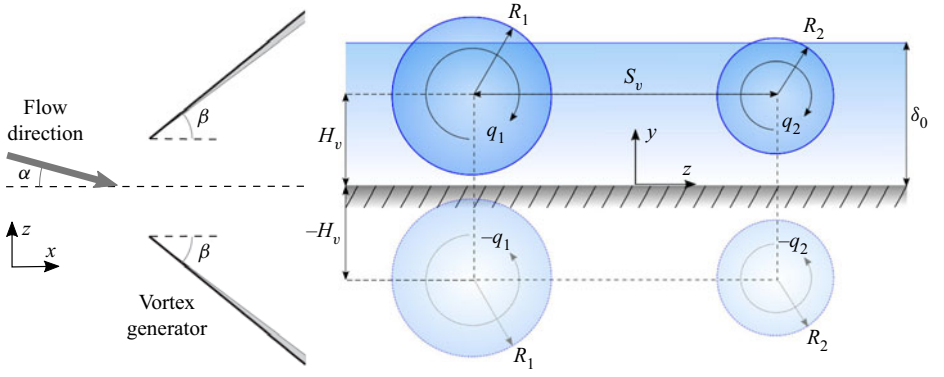

Figure 3. Diagram showing the set-up of the vortex pair at the inlet to the LES region and the definition of the parameters used in their creation.

Mesh	L_x	$\Delta x+$	N_x	L_y	$y+$	N_y	L_z	$\Delta z+$	N_z
RANS ZPG TBL	$402\delta_0$	—	545	$172\delta_0$	1	385	—	—	1
WMLES ZPG TBL	$113\delta_0$	100–200	587	$52\delta_0$	1	126	$5\delta_0$	50	103
WMLES ZPG TBL + VG	$113\delta_0$	100–200	587	$52\delta_0$	1	136	$12.5\delta_0$	50	255
WMLES ZPG TBL + VG coarse	$113\delta_0$	125–250	466	$52\delta_0$	1	108	$12.5\delta_0$	63	202

Table 1. Properties of the meshes used for both cases.

(Mockett *et al.* 2017), and focus on capturing accurately the outer part of the boundary layer at an efficient resolution. The main mesh characteristics for the WMLES cases with and without vortices included are presented alongside those of the RANS mesh in table 1.

For the LES calculations, the total number of grid points is $N_{xyz} \approx 7.6 \times 10^6$ for the mesh used for the turbulent boundary layer only. When the vortices are introduced, the domain size is increased in the spanwise direction from $5\delta_0$ to $12.5\delta_0$ in order to capture the vortices as they develop downstream; this specific width is chosen to match the width of the domain used in the reference study by Liu *et al.* (1996). Additional refinement is also included in the y-direction to account for the slight increase in boundary layer height, which leads to a larger mesh of size $N_{xyz} \approx 20 \times 10^6$. The wall-normal grid size for the turbulent boundary layer flow and the corresponding blending behaviour is shown to be performing as designed in § 3. The sensitivity to the grid spacing with the inclusion of vortices is shown through the comparison of the vortex development on different grids in § 4.1.

3. Zero pressure gradient turbulent boundary layer

In order to verify the proposed methodology, an initial investigation was conducted on a ZPG turbulent boundary layer free from the influence of vortices. The free stream velocity in this case is $U_0 = 70\,\mathrm{m\,s^{-1}}$, with viscosity $\nu = 1.48305 \times 10^{-5}\,\mathrm{m^2\,s^{-1}}$, resulting in a Reynolds number per metre $Re/x = 4.72 \times 10^6\,\mathrm{m^{-1}}$. From the precursor RANS calculation, the mean flow and turbulence statistics were taken in order to produce the inlet condition for the LES region.

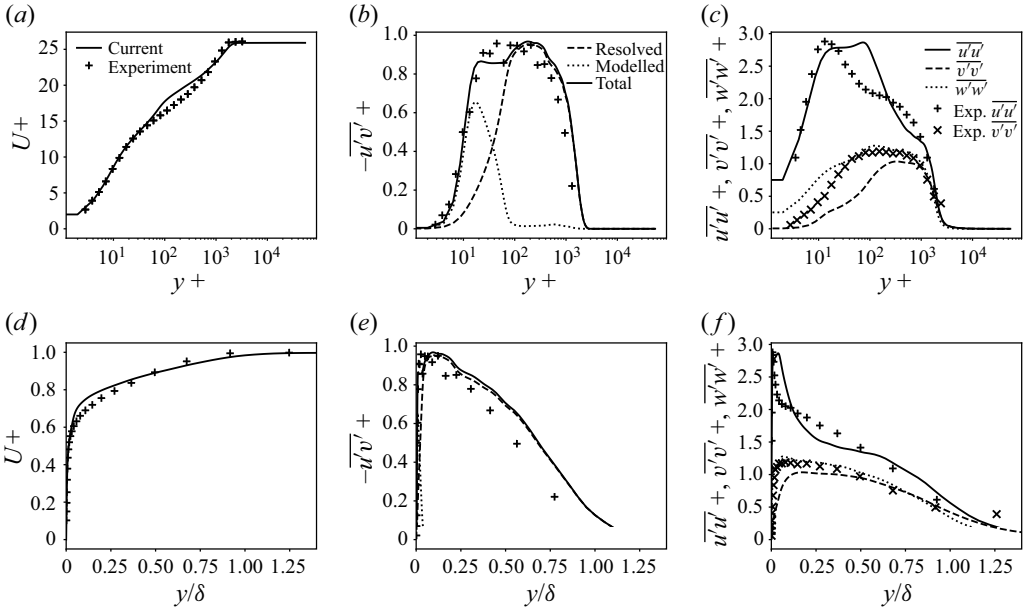

Figure 4. Velocity and Reynolds stress profiles at $Re_\theta = 5200$, with crosses showing experimental data from DeGraaff & Eaton (2000). Profiles are given in (*a–c*) wall units and (*d–f*) outer units.

The LES domain is selected to begin at the point in the domain where the Reynolds number based on the momentum thickness (θ) of the boundary layer is $Re_{\theta_0} = U_0\theta_0/\nu = 3040$, and the initial boundary layer thickness is $\delta_0 = 5.8 \times 10^{-3}$ m.

The profile of mean streamwise velocity (U) is compared to experimental data from DeGraaff & Eaton (2000) at a downstream location where $Re_\theta = 5200$, as shown in figure 4, along with profiles of the turbulence shear and normal stresses. The quantities denoted with a $+$ are normalised by the wall friction velocity $u_\tau = \sqrt{\tau_w/\rho}$, where the wall shear stress is $\tau_w = \partial u/\partial y|_w$, and are plotted over the distance from the wall in wall units $y+ = yu_\tau/\nu$ to display the values close to the wall, and with outer units y/δ to show the performance away from the wall. The turbulence model is active in the near-wall region, up to $y+ \approx 100$, after which there is a switch to LES, and the modelled shear stress drops to zero. A small velocity mismatch in the log layer corresponds to this switch from RANS to LES, which is characteristic of this model and due to the low resolution in the near-wall region (see e.g. Gritskevich, Garbaruk & Menter 2017). The LES framework is otherwise shown to calculate accurately the first and second moment statistics of the turbulent flow, particularly in the outer region $y/\delta > 0.1$, corresponding approximately to $y+ > 200$, which is the region where the vortex will be introduced.

Downstream of the inlet, the imposed synthetic fluctuations rapidly bring about the resolution of realistic turbulent structures in the outer region, where the LES is active, as shown in figure 5. This can be seen by the fast convergence of the power spectral density (PSD) plot with streamwise location. This adjustment period occurs at a slower rate in the inner layer since the SEM is not active in the RANS region near the wall. To measure the 'recovery length' at the wall, the coefficient of friction $C_f = \tau_w/(0.5\rho U_0^2)$ is plotted along the length of the plate in figure 5. There is an initial drop in C_f at the very start, due to a lack of prescribed turbulence in this region, before the flow recovers and C_f returns to match the DNS (Schlatter & Örlü 2010) and experimental (DeGraaff & Eaton 2000;

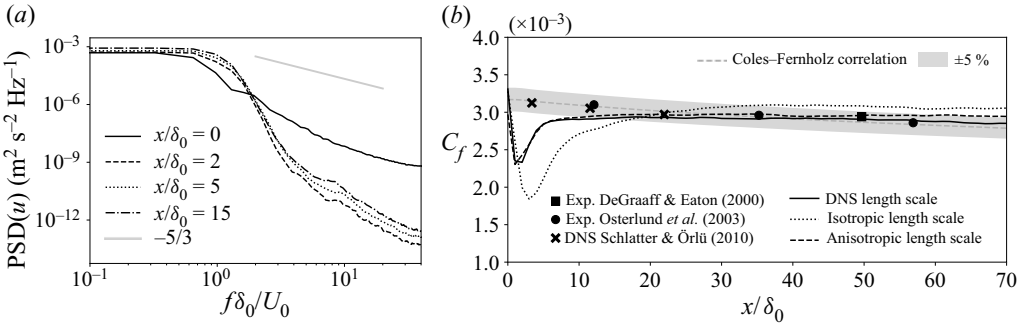

Figure 5. (*a*) Power spectral density (PSD) of the streamwise velocity, sampled at a height $y = 0.5\delta_0$, for various downstream locations. (*b*) Coefficient of friction along the length of the domain showing the development length for the different length scale definitions compared to DNS data, experimental data and the Coles–Femholz correlation.

Osterlund, Lindgren & Johansson 2003) values. In order to reduce the recovery length required for the development of the turbulence statistics, an investigation into the effect of the prescribed length scales in each direction, $\boldsymbol{\sigma}_i$, used in the generation of the turbulent structures by the SEM, was conducted. In this study, this quantity is taken to be one of the forms

$$\boldsymbol{\sigma}_i = \frac{k^{3/2}}{\varepsilon} \quad \text{or} \quad \boldsymbol{\sigma}_i = \frac{\boldsymbol{R}_{ii}^{3/2}}{\varepsilon}, \tag{3.1}$$

where k is the turbulence kinetic energy, ε is the turbulence time scale, and $\boldsymbol{R}_{ii}$ are the normal turbulence stresses, with the subscript i denoting the direction (x, y, z). These give either an isotropic or an anisotropic eddy shape, respectively. As a linear Boussinesq representation is used in the RANS domain, the Reynolds stresses are calculated for the flat plate using the Wilcox hypothesis as follows, as suggested in Laraufie & Deck (2013):

$$R_{xx} = \frac{4}{9}2k, \quad R_{yy} = \frac{2}{9}2k, \quad R_{zz} = \frac{1}{9}2k. \tag{3.2a-c}$$

Figure 6 presents the different length scales employed with the SEM at the inlet to the LES domain at $Re_\theta = 3040$. Also shown is the length scale calculated using (3.1) but with the $\boldsymbol{R}_{ii}$ values taken from the DNS data of Schlatter & Örlü (2010) to give a more accurate definition for comparison. Figure 5 indicates that the development length is significantly shortened by the introduction of an anisotropic length scale when compared to an isotropic length scale. Furthermore, the results using the Wilcox length scale are very similar to those when using DNS data, which indicates that the former is sufficient for this flow. Further cases presented here therefore use the Wilcox anisotropic length scale definition. The approximate development length determined from figure 5 is highlighted in relevant future plots by the shaded region at the start of the domain.

4. The incorporation of vortex pairs

4.1. *Validation of method*

The central focus in this paper is the vortex generator study reported by Pauley & Eaton (1988), later replicated numerically by Liu *et al.* (1996) using LES with a rescaling method proposed by Spalart & Watmuff (1993) to rescale the spatially developing boundary layer

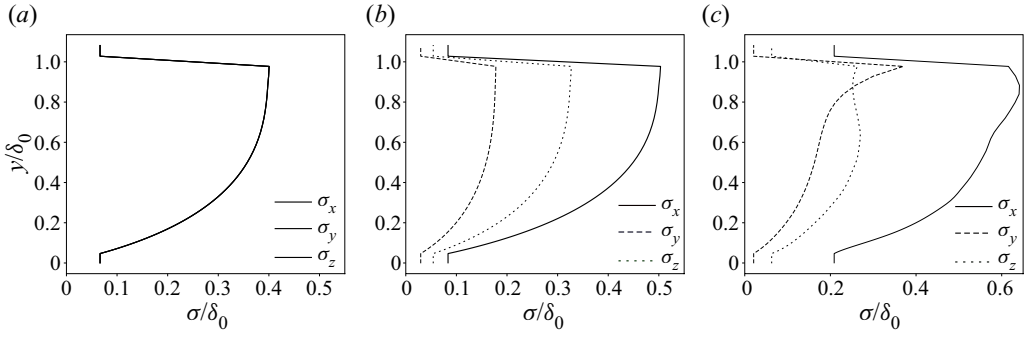

Figure 6. Length scale definitions used in the SEM inlet condition varying in the wall-normal direction reconstructed using (*a*) an isotropic length scale, (*b*) an anisotropic length scale (from Laraufie & Deck 2013), and (*c*) a DNS length scale (from Schlatter & Örlü 2010).

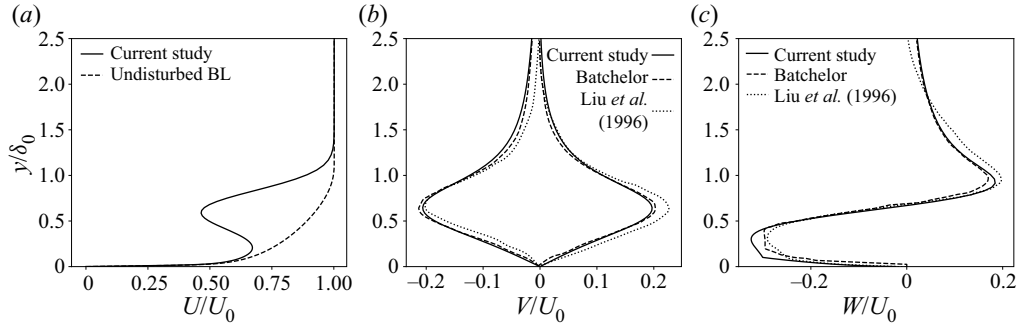

Figure 7. The mean velocity components in the *x*-, *y*- and *z*-directions applied at the inlet to the LES domain compared to a Batchelor vortex and the inlet used by Liu *et al.* (1996). The profiles of U and W are located at the vortex core location in the *z*-direction, and the V profiles are shown to each side of the vortex core.

in a periodic domain. They introduced the vortex pairs using a body force of a similar field as that used in the present work, described in § 2.3. In the current study, the Batchelor vortices are applied at the location corresponding to the first measurement point in the experiment, immediately downstream of the vortex generator. These vortices, henceforth referred to as the primary vortices, were generated with a separation distance $S_v = 11\delta_0/4$, at height above the wall $h_v = 5\delta_0/8$, with radii $R_1 = R_2 = 2.1\delta_0/8$ and the vortex strength in (2.2), $q_1 = -q_2 = 0.37U_0$. These setting were selected to match the velocity profiles used by Liu *et al.* (1996), as shown in figure 7. These profiles match closely between the current method of applying the vortices to the velocity field of the inlet and the method of applying a body force used by Liu *et al.* (1996). In (2.3), q_w is set as $1.25|q|$ so that the local minimum streamwise velocity, at the vortex core, is $u = 0.45U_0$, matching the value in the experiment (Liu *et al.* 1996).

Downstream of the inlet, the development of the peak streamwise vorticity ω_x^{max}, where the vorticity is defined as the curl of the velocity field $\boldsymbol{\omega}_i = \nabla \times \boldsymbol{u}_i$, is shown along the length of the plate in figure 8. This is compared to corresponding values reported in both previous LES and experimental studies. The peak vorticity decay closely matches that reported by Liu *et al.* (1996). In both the present work and the results of Liu *et al.*, the vortex diffuses at a slightly greater rate than the experiment, particularly in the region $x/\delta_0 > 20$. This discrepancy may be due to different levels of turbulence present

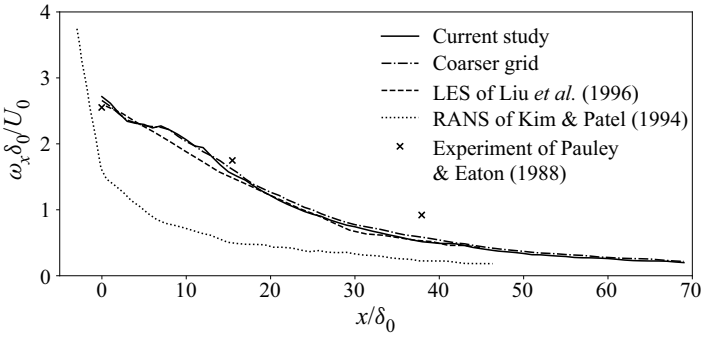

Figure 8. The evolution of the peak streamwise vorticity along the streamwise direction compared to Liu *et al.* (1996), Kim & Patel (1994) and Pauley & Eaton (1988).

in the experiment. In contrast, the reference RANS results from Kim & Patel (1994), reproduced in figure 8, can be seen to drastically under-predict this quantity. It is well established that standard RANS models, based on the linear Boussinesq hypothesis, fail to capture the turbulence at the vortex core, which arises due to the direct link between mean strain rate and turbulence Reynolds stresses. Excessive turbulence levels diffuse the momentum, thus the vorticity is reduced. More recent RANS results from Spalart *et al.* (2015) demonstrated some improvement by incorporating curvature correction, but still found an over-prediction in the downstream diffusion of the vortex, and subsequently lower levels of vorticity. The results of the coarser grid in figure 8 give confidence in the results obtained with the mesh at higher resolution.

Further detailed comparison is presented in figure 9, showing a slice through the primary vortices at location $15\delta_0$ downstream of the inlet. At this location, the contours of a number of second-order statistics were plotted: the turbulence shear stress $-\overline{u'v'}$, the turbulence kinetic energy $k = 0.5(\overline{u'u'} + \overline{v'v'} + \overline{w'w'})$, and the turbulence anisotropy $-(\overline{v'v'} - \overline{w'w'})$. These are compared to the same plots from both the LES and experimental studies (Pauley & Eaton 1988; Liu *et al.* 1996). The position, size and levels of the contours are observed to be in strong agreement with experimental results, slightly more so than those reported in the LES study of Liu *et al.*, particularly if one examines the spanwise position of the primary vortex. The contours of the turbulence shear stress highlight a region of positive shear stress at the core, i.e. where $-\overline{u'v'} < 0$.

Line plots at this station ($x = 16\delta_0$) for the mean velocity components and the turbulence shear stress are shown in Figure 10, comparing the results to those of a coarser mesh defined in table 1. These show that the first-order statistics of the flow are independent of the mesh. From this point onwards, the standard mesh with cells $N_{xyz} \approx 20 \times 10^6$ is used for all results.

4.2. *Counter-rotating, co-rotating and single-vortex flows*

Once validated, the Batchelor vortex used to model the effects of the vortex generator can be adjusted easily, as described in § 2.3. This allows for a range of other vortex generator configurations to be investigated with relative ease by varying the parameters shown in figure 3. In the present subsection, results for a series of cases representing both counter-rotating and co-rotating vortex pairs and a single vortex are presented and discussed. The vortex properties used in these cases are given in table 2.

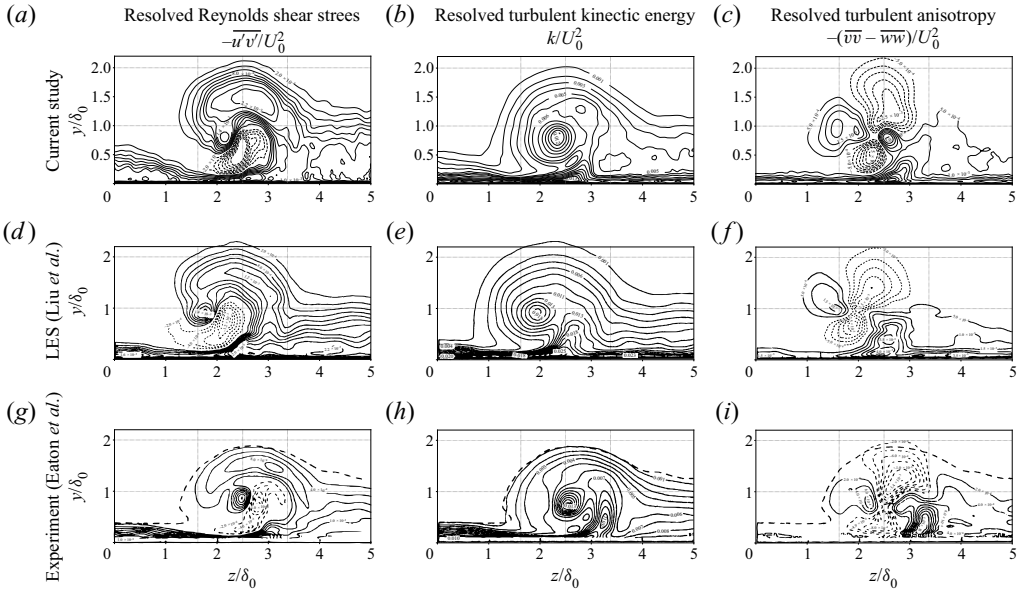

Figure 9. Contour plots at location $x = 16\delta_0$ showing the computed (*a*,*d*,*g*) turbulence shear stress, (*b*,*e*,*h*) turbulence kinetic energy, and (*c*,*f*,*i*) turbulence anisotropy for (*a–c*) the current study, compared to (*d–f*) the previous LES study (Liu *et al.* 1996) and (*g–i*) the experimental study (Pauley & Eaton 1988). (Solid lines show positive contours, and dashed lines show negative contours.)

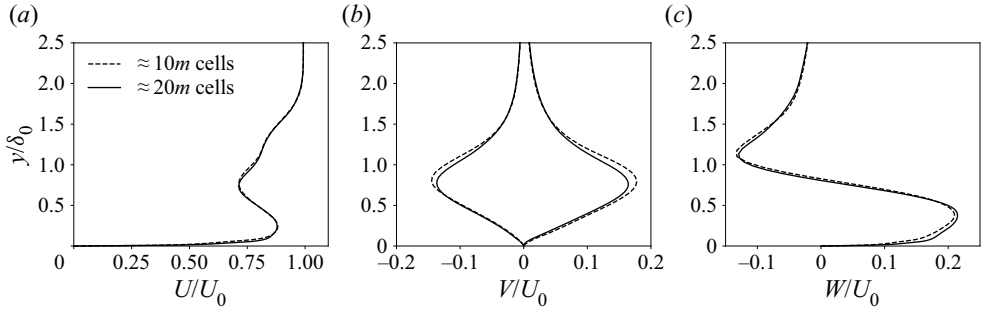

Figure 10. Line plots at location $x = 16\delta_0$ showing the mean velocity components computed using the standard and coarse meshes. The profiles of U and W are located at the vortex core location in the z-direction, and the V profiles are shown to each side of the vortex.

Case no.	Rotation	H_v	S_v	R_1	R_2	q_1	q_2
C1	Counter-rotating	$0.625\delta_0$	$1.75\delta_0$	$0.263\delta_0$	R_1	$0.37U_0$	$-q_1$
O1	Co-rotating	$0.625\delta_0$	$1.75\delta_0$	$0.263\delta_0$	R_1	$0.37U_0$	q_1
S1	Single vortex	$0.625\delta_0$	—	$0.263\delta_0$	—	$0.37U_0$	—

Table 2. Properties of baseline counter-rotating, co-rotating and single-vortex flows.

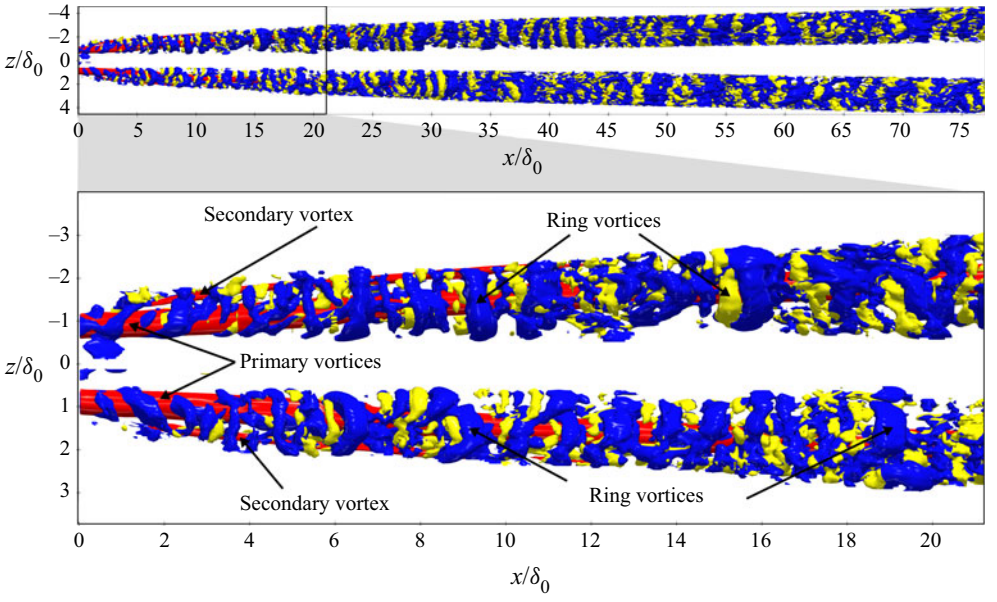

Figure 11. Isocontours of the second invariant of the velocity gradient tensor (Q) for the C1 case. Mean flow contours are shown in red, and instantaneous contours are coloured blue and yellow for negative and positive spanwise vorticity (ω_z), respectively.

To start with, we compare three baseline cases, here referred to as case C1, the counter-rotating pair considered in § 4.1, case O1, which has the same set-up but with co-rotating vortices, and case S1, with a single vortex having the same strength and starting location.

4.2.1. *Flow structure*

Figures 11–13 display a visualisation of the flow in cases C1, O1 and S1, respectively. The plots include both Q-isocontours calculated from the instantaneous and time-averaged velocity:

$$Q_{inst} = \frac{1}{2}\left((\nabla \cdot \langle \boldsymbol{u}_i \rangle)^2 - \nabla \langle \boldsymbol{u}_i \rangle : \nabla \langle \boldsymbol{u}_i \rangle^{\mathrm{T}}\right), \tag{4.1}$$

$$Q_{mean} = \frac{1}{2}\left((\nabla \cdot \overline{\langle \boldsymbol{u}_i \rangle})^2 - \nabla \overline{\langle \boldsymbol{u}_i \rangle} : \nabla \overline{\langle \boldsymbol{u}_i \rangle}^{\mathrm{T}}\right). \tag{4.2}$$

Contours of $Q_{mean} = 2 \times 10^6$ are shown in red. These highlight the development of the mean vortices introduced by using the Batchelor vortex model as described in (2.2). The formation of a secondary, smaller vortex can be seen as the primary vortex interacts with the wall. Contours of $Q_{inst} = 1 \times 10^5$ are clipped to show only those where the mean spanwise velocity is $U_z > 5$ in the direction of the vortex, to highlight the instantaneous turbulent structures present over the top of the main vortex. The introduction of the turbulent structures at the inlet, and their interaction with the vortices, can be seen clearly. We also observe the formation of pairs of counter-rotating ring vortices, encircling the primary vortex highlighted in figures 11–13. These structures are coloured yellow and blue with positive and negative values of ω_z, respectively. Initially, these ring vortices remain relatively coherent and grow in strength, before subsequently breaking down, due to both

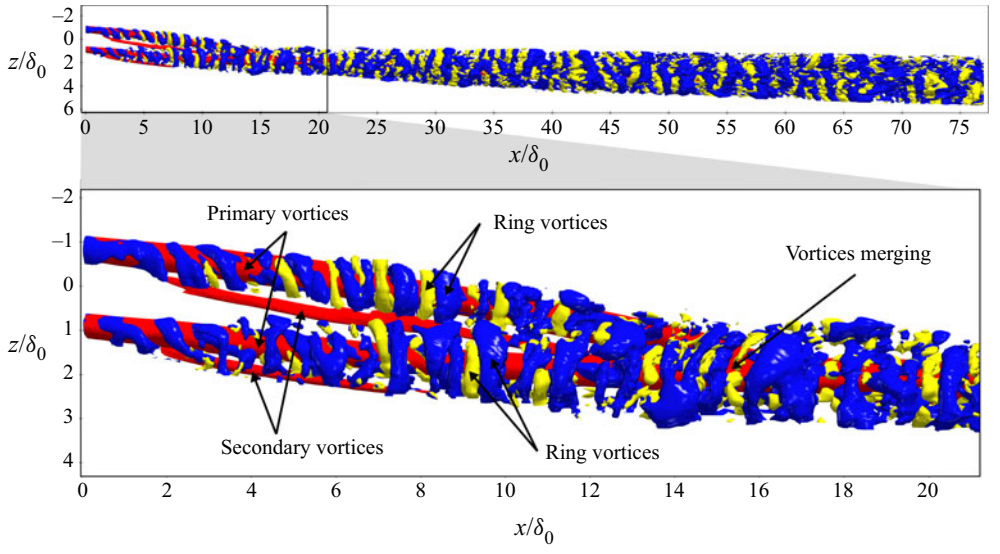

Figure 12. Isocontours of the second invariant of the velocity gradient tensor (Q) for the O1 case. Mean flow contours are shown in red, and instantaneous contours are coloured blue and yellow for negative and positive spanwise vorticity (ω_z), respectively.

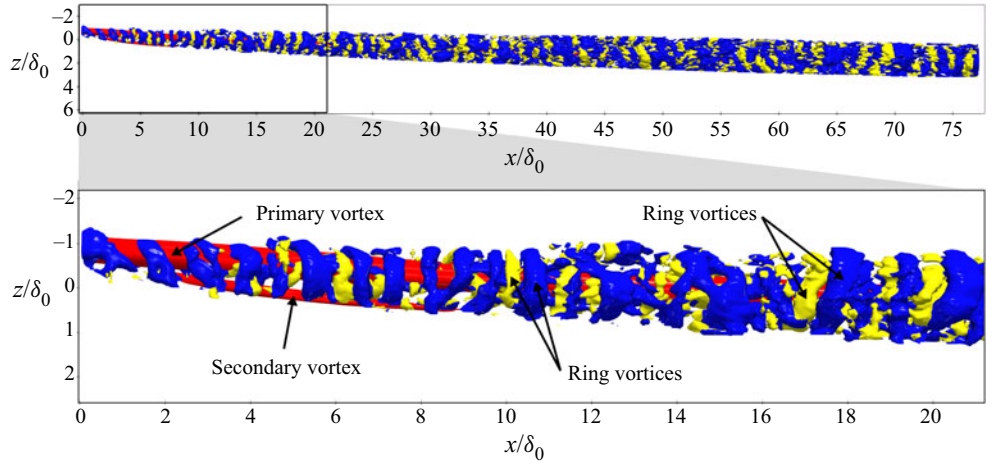

Figure 13. Isocontours of the second invariant of the velocity gradient tensor (Q) for the S1 case. Mean flow contours are shown in red, and instantaneous contours are coloured blue and yellow for negative and positive spanwise vorticity (ω_z), respectively.

vortex–vortex and vortex–turbulence interactions. In the O1 case shown in figure 12, the two primary co-rotating vortices merge at location $\approx 15\delta_0$.

Figures 14(a,b) display the trajectories of the vortex cores from plan and side views, respectively. All vortices remain within the boundary layer for the full extent of the domain. As well as spreading apart, the counter-rotating vortices rise up within the boundary, although they do not rise as high as a single vortex, suggesting that the proximity to the counter-rotating vortex is holding them closer to the wall. The co-rotating

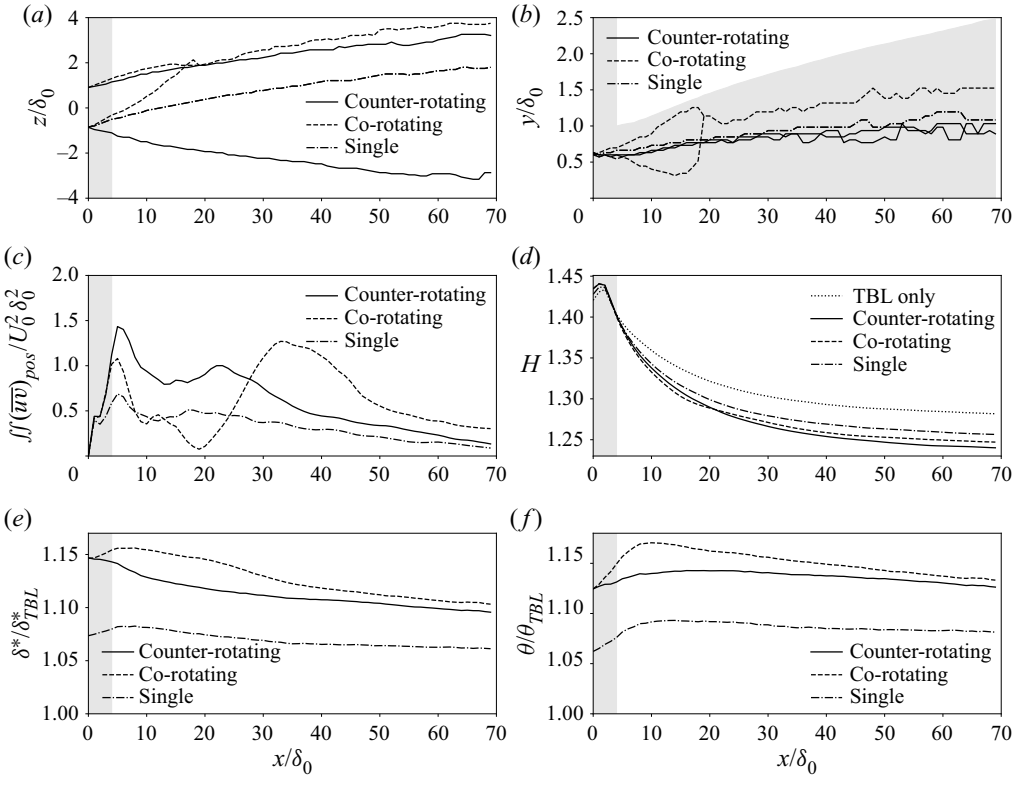

Figure 14. Trajectory of the vortex cores along the length of the developing boundary layer for cases C1, O1 and S1, for (*a*) plan view and (*b*) side view. The grey region at the start of the domain represents the SEM development region. In the side view plot, the boundary layer thickness (δ) of an undisturbed boundary layer is shown in light grey for reference. (*c*) Integral of the positive shear stress over a plane. (*d*) Average shape factor along the length of the boundary layer. (*e*,*f*) Displacement and momentum thicknesses separately normalised by the case with no vortices present.

vortices combine and migrate to one side, while they also rise significantly higher than the counter-rotating pair, before settling just below the edge of the boundary layer.

The shape factor H is also plotted in figure 14(*d*) for these cases. This quantity, the ratio of the displacement thickness δ^* to momentum thickness θ, provides a measure of how close to the wall the momentum is contained. A lower value of H therefore represents a more effective vortex generator configuration. Note that the quantity is averaged over a spatial region equal to the full xz plane. It can be seen that the co-rotating pair, case O1, initially exhibits the lowest H, due perhaps to the movement of the smaller vortex towards the wall. At the point where the vortices merge, the co-rotating pair becomes less effective at transferring momentum to the vicinity of the wall, since the combined vortex settles in a location higher in the boundary layer than for the counter-rotating case C1. In all three cases, it can be seen that the shape factor is significantly lower than that of an undisturbed turbulent boundary layer. In the separate plots of displacement and momentum thickness shown in figures 14(*e*,*f*), respectively, it is shown that both thicknesses initially rise for the co-rotating and single vortices, whereas they initially drop for the counter-rotating case. This drop for the counter-rotating case can be attributed to the growing area of thinned boundary layer between the two vortices that is not present in the other cases. Case S1 is

less effective at transferring momentum towards the wall, likely as with a single vortex the total circulation introduced is also lower. Figure 14(*c*) also displays a plot of the total positive shear stress over a plane, $\iint(\overline{u'v'})_{pos}$, along x, which is referred to later on.

4.2.2. *Vorticity and shear stress*

Figures 15–17 describe the downstream development of axial vorticity and both streamwise and spanwise shear stresses, for cases C1, O1 and S1, respectively. For case C1, shown in figure 15, the vorticity contours show how the primary vortices interact with the wall and generate secondary vortices near the wall. These secondary vortices are then pulled outwards and away from the wall by the primary vortices. The primary vortices reduce in strength and gradually move apart along the length of the boundary layer.

The turbulence shear stress contour plots show that there is an area of considerable boundary layer thinning between the vortices. This is a good indication for the performance of the vortex generator in its ability to transfer momentum from the free stream closer to the wall and therefore delay the onset of potential separation. Also highlighted is the presence of an area of positive shear stress, shown in red. As discussed previously, this is an important factor in the preservation of the vortex, with the corresponding destruction of turbulence in the region slowing the diffusion of the vortex.

The contours of vorticity plots shown in figure 16 show a co-rotating vortex pair. In this case, both vortices initially move in the same direction before merging to form a single vortex from around $x = 20\delta_0$. The merging of the vortices can also be seen in figure 14. It can be seen that the vortex starting at location $z = -7\delta_0/8$ is pulled closer to the other vortex whilst also descending lower within the boundary layer. Conversely, the vortex that starts at location $z = 7\delta_0/8$ moves upwards. The lower vortex then passes underneath the other one before they combine at around $x = 20\delta_0$. Once the vortices have merged to form a single vortex, it continues to slowly move away from the wall at a height larger than that of the counter-rotating pair but still within the height of an undisturbed boundary layer.

It can be seen from the contour plots of turbulence shear stress in figure 16 that at the point where the vortices merge, at $x = 20\delta_0$, there is a significant drop in the positive shear stress. This is likely due to the increased shear flow that occurs as the two vortices approach each other. It can be seen in the contour plots in figure 16 that there is an area of strong, negative shear stress between the two vortex cores, supporting this hypothesis. In order to better assess this property, the shear stress is integrated in the area in the yz plane where it is positive. This metric, $\iint(\overline{u'v'})_{pos}$, is then plotted against the streamwise direction and is shown for cases C1, O1 and S1 in figure 14. For the co-rotating vortex pairs, this shows a drop in positive shear stress as the vortices merge, followed by a significant rise.

4.2.3. *Turbulence anisotropy and production*

It is instructive to consider in more detail the nature of the observed levels of turbulence, both to aid the interpretation of the flow physics and to help us to understand RANS modelling of this flow. As discussed in § 1, previous attempts to use RANS models for these flows have demonstrated an inability to predict physics in the vortex core region. In this subsubsection, we consider the anisotropy of the turbulence, defined by

$$\boldsymbol{a}_{ij} = \frac{\overline{\boldsymbol{u}_i'\boldsymbol{u}_j'}}{2k} - \frac{\boldsymbol{\delta}_{ij}}{3}, \tag{4.3}$$

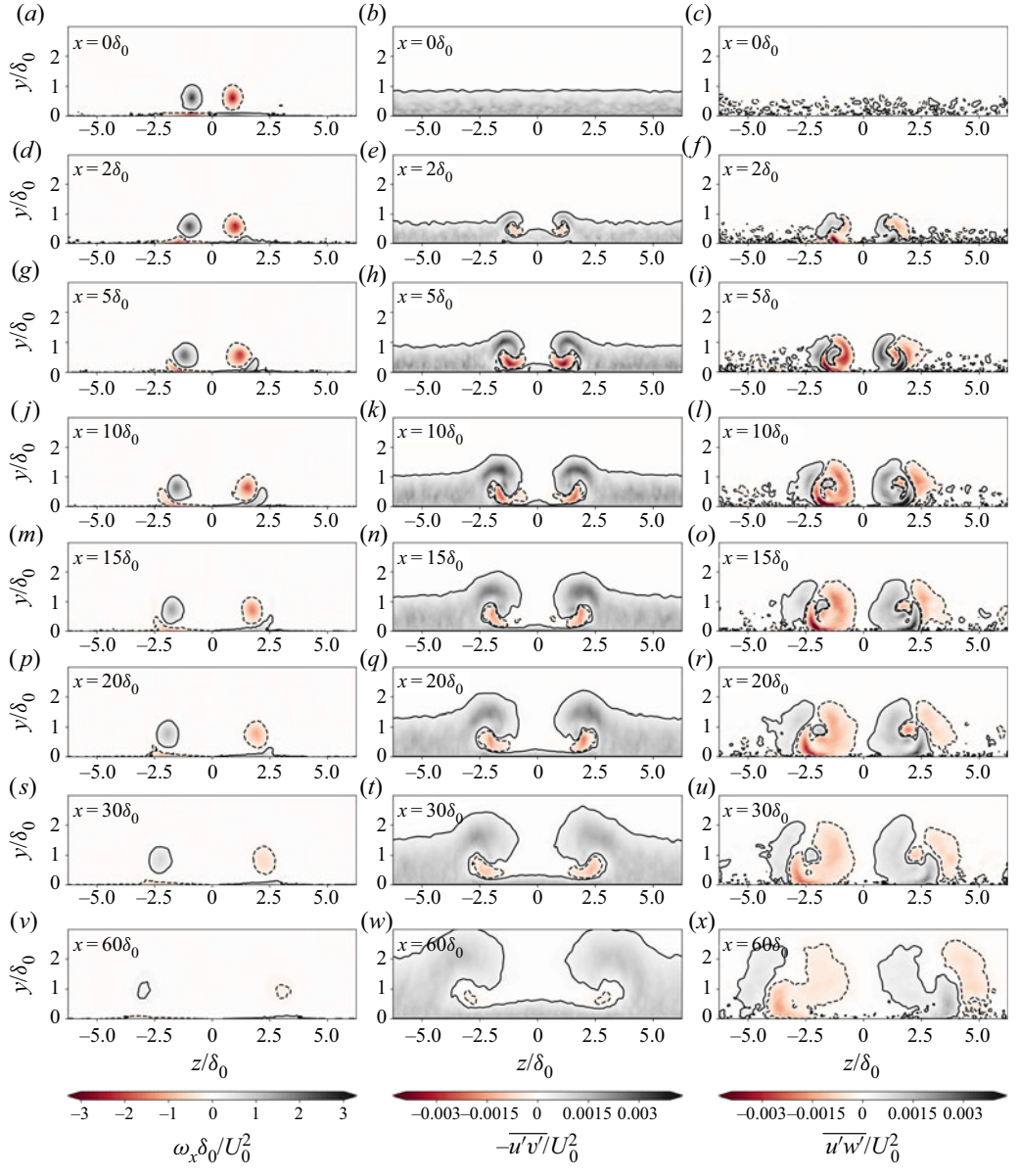

Figure 15. Contour plots for case C1, showing (*a*,*d*,*g*,*j*,*m*,*p*,*s*,*v*) the streamwise vorticity, and the turbulence shear stresses (*b*,*e*,*h*,*k*,*n*,*q*,*t*,*w*) $\overline{u'v'}$ and (*c*,*f*,*i*,*l*,*o*,*r*,*u*,*x*) $\overline{u'w'}$, with slices in the *yz* plane taken at locations $x/\delta_0 = 0, 2, 5, 10, 15, 20, 30, 60$.

where $\boldsymbol{\delta}_{ij}$ is the Kronecker delta function

$$\boldsymbol{\delta}_{ij} = \begin{cases} 1, & \text{if } i = j, \\ 0, & \text{otherwise.} \end{cases} \tag{4.4}$$

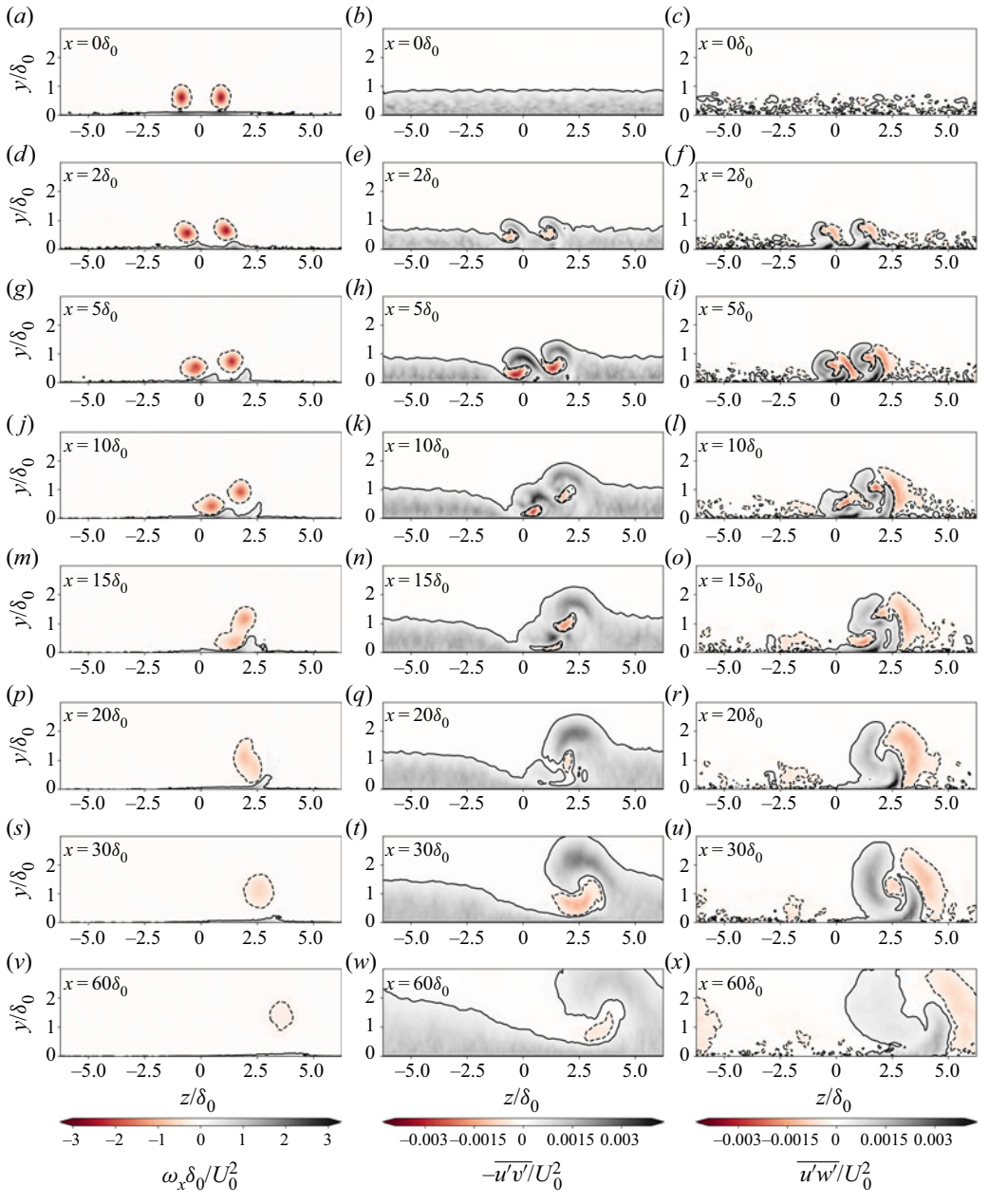

Figure 16. Contour plots for case O1 showing (*a*,*d*,*g*,*j*,*m*,*p*,*s*,*v*) the streamwise vorticity, and and the turbulence shear stresses (*b*,*e*,*h*,*k*,*n*,*q*,*t*,*w*) $\overline{u'v'}$ and (*c*,*f*,*i*,*l*,*o*,*r*,*u*,*x*) $\overline{u'w'}$, with slices in the *yz* plane taken at locations $x/\delta_0 = 0, 2, 5, 10, 15, 20, 30, 60$.

Also presented is the production of the turbulence kinetic energy which is calculated as

$$P_k = \overline{\boldsymbol{u}_i' \boldsymbol{u}_j'} \frac{\partial \boldsymbol{U}_i}{\partial \boldsymbol{x}_j}. \tag{4.5}$$

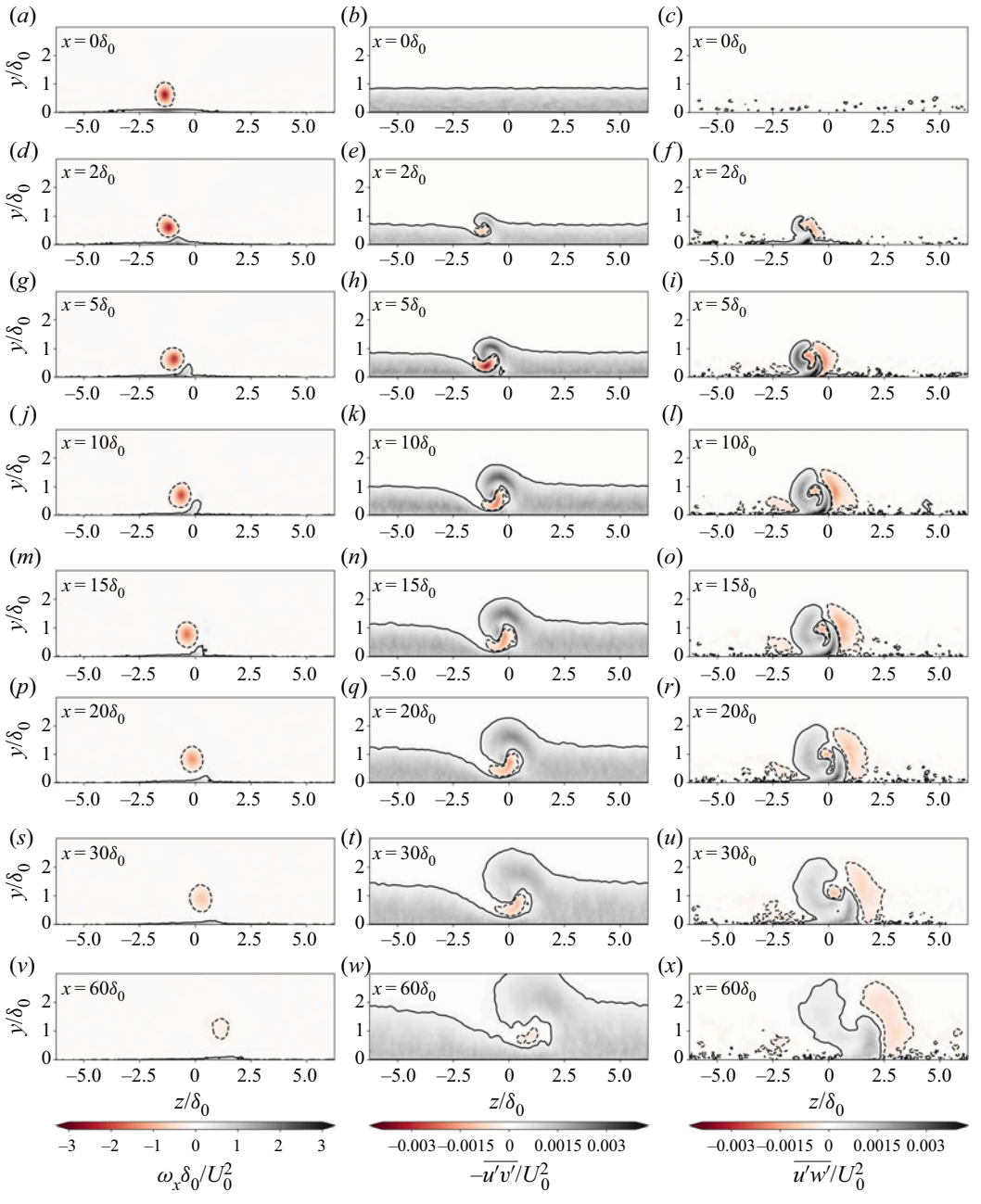

Figure 17. Contour plots for case S1 showing (*a*,*d*,*g*,*j*,*m*,*p*,*s*,*v*) the streamwise vorticity, and and the turbulence shear stresses (*b*,*e*,*h*,*k*,*n*,*q*,*t*,*w*) $\overline{u'v'}$ and (*c*,*f*,*i*,*l*,*o*,*r*,*u*,*x*) $\overline{u'w'}$, with slices in the yz plane taken at locations $x/\delta_0 = 0, 2, 5, 10, 15, 20, 30, 60$.

In figures 18–20, we display these quantities for cases C1, O1 and S1, respectively. The anisotropy is plotted using the colour map method proposed by Emory & Iaccarino (2014). In this method, the componentality of the turbulence anisotropy at each point of the domain is allocated an RGB colour by mapping the eigenvalues λ_i of the anisotropy

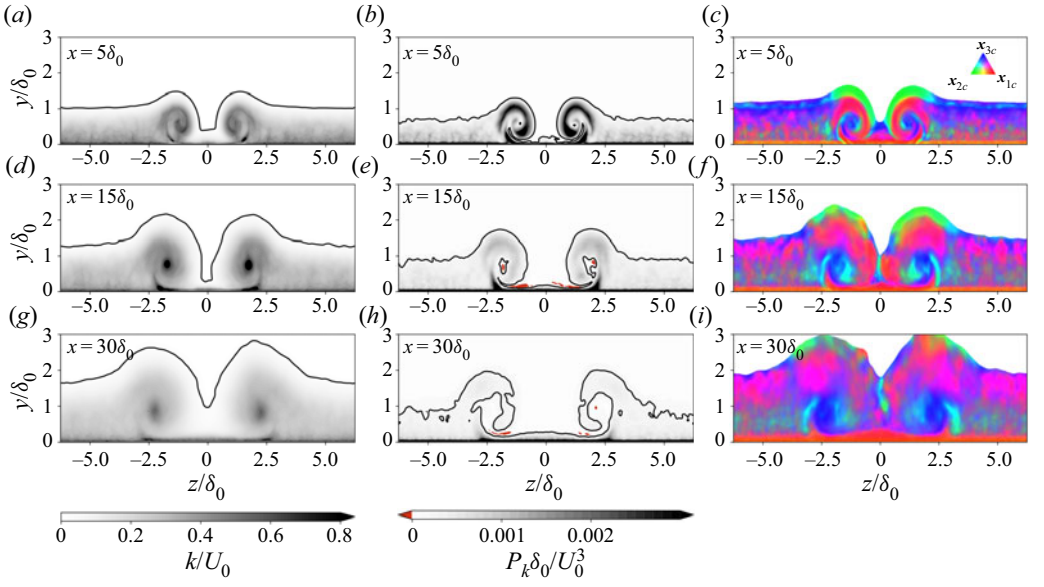

Figure 18. Contour plots for case C1 of (*a*,*d*,*g*) turbulence kinetic energy k, (*b*,*e*,*h*) production of k, P_k, and (*c*,*f*,*i*) anisotropy componentality. Slices are in the yz plane at locations $x/\delta_0 = 5, 15, 30$.

tensor (a_{ij}) onto a barycentric map and assigning an RGB colour value to each position on this map:

$$\begin{bmatrix} \mathrm{R} \\ \mathrm{G} \\ \mathrm{B} \end{bmatrix} = C_{1c}^* \begin{bmatrix} 1 \\ 0 \\ 0 \end{bmatrix} + C_{2c}^* \begin{bmatrix} 0 \\ 1 \\ 0 \end{bmatrix} + C_{3c}^* \begin{bmatrix} 0 \\ 0 \\ 1 \end{bmatrix}, \tag{4.6}$$

where

$$C_{ic}^* = (C_{ic} + C_{off})^{C_{exp}}, \quad C_{1c} = \lambda_1 - \lambda_2, \quad C_{2c} = 2(\lambda_2 - \lambda_3), \quad C_{3c} = 3\lambda_3 + 1. \tag{4.7a-d}$$

The constants used to define the colour map are $C_{off} = 0.55$ and $C_{exp} = 5$, such that distinct colours represent the three corners of the colour map (red, green and blue representing one component, axisymmetric two-component and isotropic turbulent structures, respectively) and the transition areas (yellow, cyan and magenta representing two-component, axisymmetric contraction and axisymmetric expansion, respectively). For clarity, a threshold is applied so that only areas of the flow where $k/U_0 > 0.005$ are shown.

The contours of production in figure 18 show that in the initial development of the vortices, a ring of high turbulence kinetic energy production is formed around the centres of the two vortices. Further downstream, at $x = 15\delta_0$, while the turbulence kinetic energy peaks at the centre of the vortices, a rapid drop in production is observed. Indeed, at the vortex core, the production takes small negative values, coloured red in the figure. This is due to the spatial lag between the Reynolds stresses and the mean strain field, and is a characteristic result of rotating turbulent flows. This leads to a reduction of turbulence in the core, which in turn helps to reduce diffusion and increase the coherence of the vortex structures downstream. This feature cannot be captured with standard, linear, RANS models without an appropriate correction term. In contrast to isolated vortices, the present configuration is more complex on account of the interaction of the vortex with

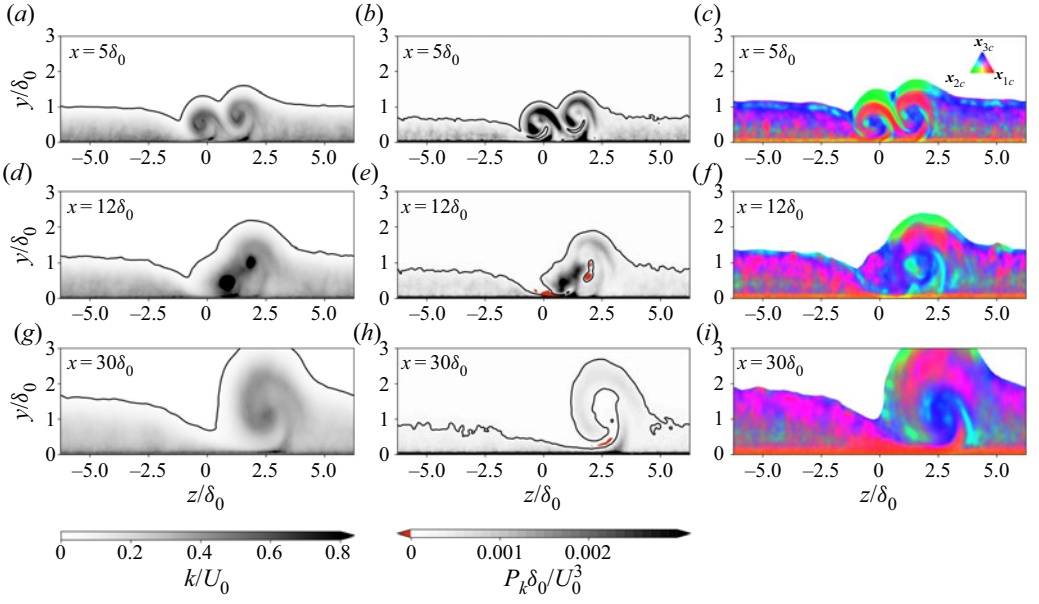

Figure 19. Contour plots for case O1 of (*a*,*d*,*g*) turbulence kinetic energy k, (*b*,*e*,*h*) production of k, P_k, and (*c*,*f*,*i*) anisotropy componentality. Slices are in the yz plane at locations $x/\delta_0 = 5$, 12, 30.

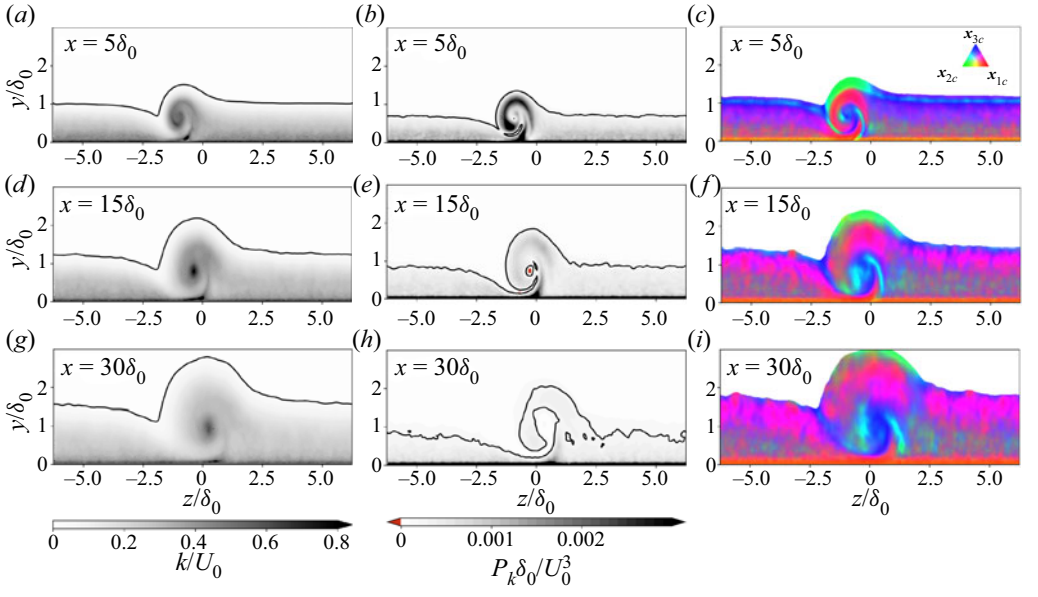

Figure 20. Contour plots for case O1 of (*a*,*d*,*g*) turbulence kinetic energy k, (*b*,*e*,*h*) production of k, P_k, and (*c*,*f*,*i*) anisotropy componentality. Slices are in the yz plane at locations $x/\delta_0 = 5$, 15, 30.

the boundary layer, which provides a continual source of turbulence kinetic energy to the vortex core. The balance of these two effects is likely to be sensitive to the distance of the vortex from the wall, amongst other factors. This effect is also observed in the S1 case in figure 20, and in the O1 case in figure 19, where it peaks as the two co-rotating vortices approach each other before merging.

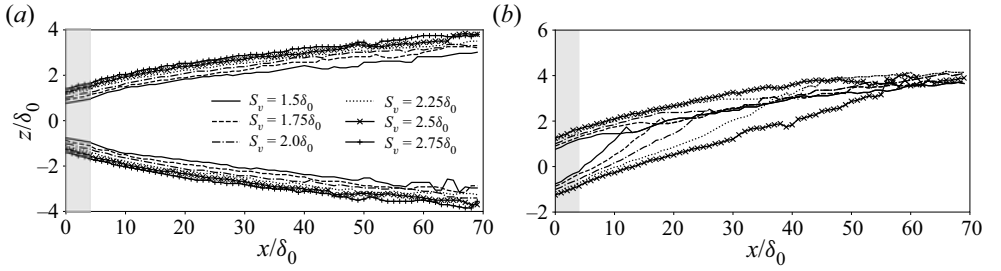

Figure 21. Plots showing how the positions of the vortex cores in the z-direction vary along the length of the developing boundary layer. The vortex paths for a range of separation distances (S_v) are shown for (*a*) co-rotating and (*b*) counter-rotating vortex pairs.

Switching focus to the anisotropy plots, it is notable, in the context of the previous paragraph, that standard linear RANS models will not be able to account for the spatial lag between Reynolds stresses and the mean strain field. Furthermore, in shear flows dominated as in the present case, they will be limited in their ability to discern Reynolds stress anisotropy, in effect limiting their applicability to the blue regions of the graph for most of this flow, in some cases possibly also part of the cyan and magenta regions. In contrast, red and green regions, respectively referring to one- and two-component states of turbulence anisotropy, are beyond standard linear RANS models. The green regions above the vortices in the anisotropy plots in figures 18–20 show how as the mean flow outside the boundary layer is pulled in by the vortices, significant areas of axisymmetric two-component turbulence are found. Much of the areas of high production, near the surface of the wall and around the centre of the vortices, corresponds to red regions of the anisotropy plot. These are areas where turbulence tends towards a one-component state that represent characteristic near-wall streaks. Similar observations are made for the three cases C1, O1 and S1, highlighting the modelling challenge presented to RANS models for flows of this nature.

4.3. *Parametric variation*

To demonstrate the flexibility of the methodology proposed in § 4.1, we proceed to examine a series of different configurations of vortex pairs. In the following we report general trends observed by varying separation distance and effective skew angle for counter-rotating vortices.

4.3.1. *Separation distance*

For both counter-rotating and co-rotating vortex pairs, the effect of the separation distance S_v on the dynamics of the vortices was investigated. The vortex paths in the xz plane are shown in figure 21. For the counter-rotating vortex pairs, the change in the separation distance at the inlet S_v correlates to a similar change in the vortex separation as they spread apart along the length of the domain. For the co-rotating pair, the inlet separation distance greatly affects the merging of the vortices; the closer together the vortices begin, the sooner they merge.

The location in the streamwise direction at which the vortices combine affects the total circulation of the vortex. This can be explained by the corresponding drop in the positive shear stress. Figure 22 shows that at the point where the vortices merge, there is a drop

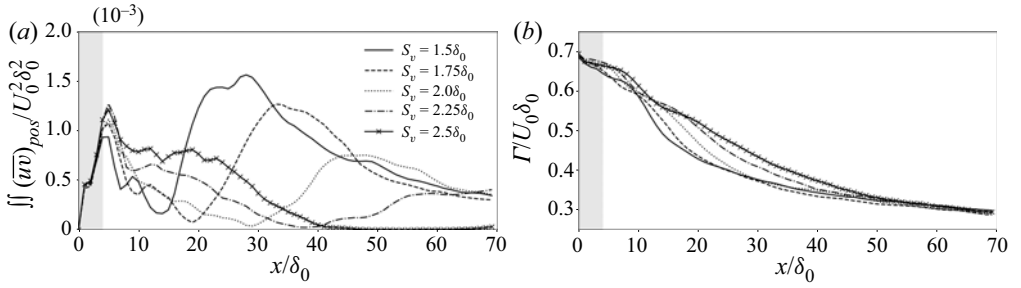

Figure 22. Plots of (*a*) the integral of the positive shear stress in a plane, (*b*) total circulation over the length of the turbulent boundary layer, for co-rotating vortices with separation distances in the range $1.5 \leq S_v/\delta_0 \leq 2.5$.

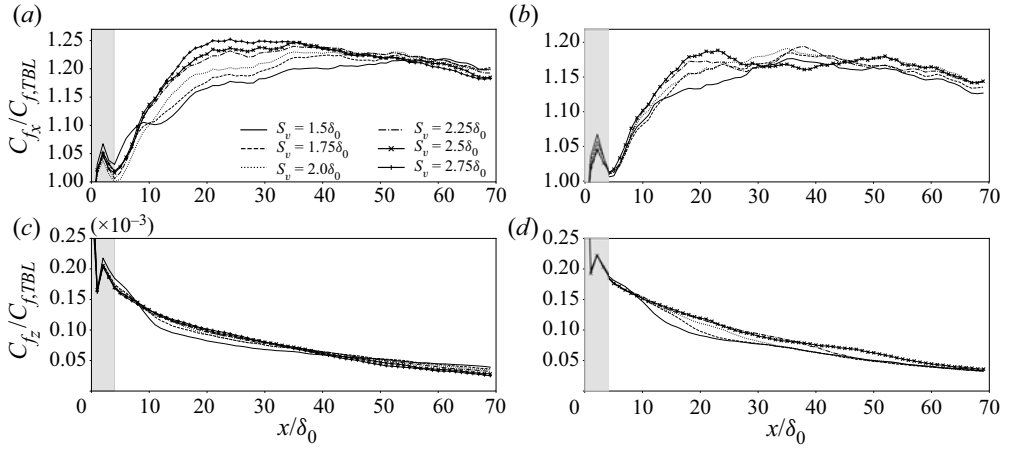

Figure 23. Plots of coefficient of friction in (*a*,*b*) the *x*-direction, and (*c*,*d*) the *z*-direction, for co-rotating vortices with various separation distances S_v. Counter-rotating vortices are shown in (*a*,*c*), and co-rotating vortices in (*b*,*d*).

in the total positive shear stress at the vortex cores. This then leads to a steeper drop in the total circulation, shown in figure 22 as the turbulence from the boundary layer acts to weaken the vortices. This in turn corresponds to a drop in the spanwise coefficient of friction (C_{f_z}) on the wall, as shown in figure 23.

For separation distances $S_v = 1.5\delta_0$, $1.75\delta_0$ and $2.0\delta_0$, there is a clear dip at the positive turbulence shear stress around the location where the vortices merge, followed by a substantial peak. However, for separation distances $S_v > 2\delta_0$, the drop in $\iint (\overline{u'v'})_{pos}$ is far more gradual. At separation distance $S_v = 2.25\delta_0$, the area of positive shear stress recovers after merging; however, for $S_v = 2.5\delta_0$, the integral drops to zero and no recovery is observed.

The effect of variable separation distance on the coefficient of friction at the wall is shown in figure 23, with both the streamwise (C_{f_x}) and spanwise (C_{f_z}) values plotted for counter-rotating and co-rotating vortices. For counter-rotating vortex pairs, a higher separation distance corresponds to a faster rise in C_{f_x}. Although a higher C_{f_x} corresponds to a higher drag force acting on the surface, it also suggests a higher resilience to separation, and shows the vortex generators working more effectively over a longer length.

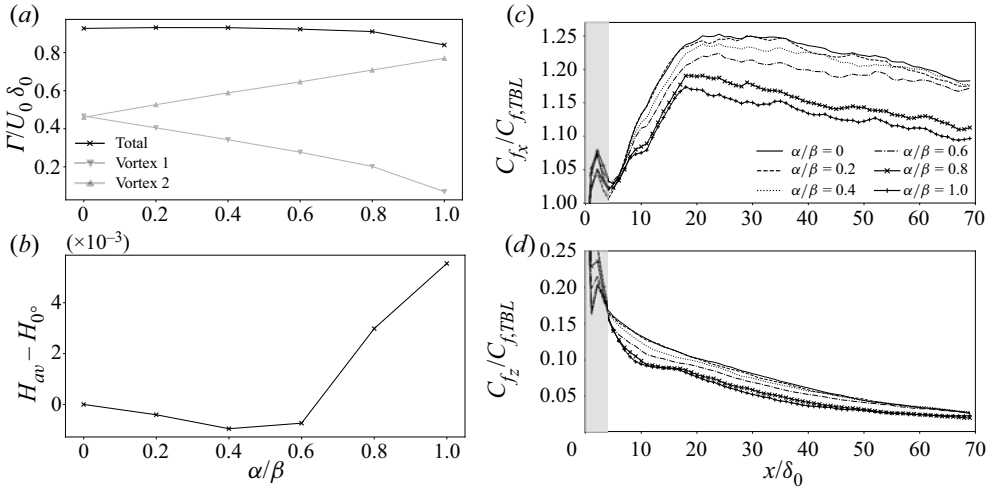

Figure 24. Plots showing (*a*) the total circulation and the circulation of the contributing vortices, and (*b*) the difference in the average shape factor introduced by the change in angle over the whole domain as the skew angle α relative to the vortex generator angle β is varied. Plots of the coefficient of friction in (*c*) the *x*-direction and (*d*) the *z*-direction, for counter-rotating vortices with skew angles in the range $\alpha/\beta = 0$–1.

Vortices starting closer together are initially less effective, although in these cases, C_{f_x} increases to levels observed in other cases further downstream as the vortices spread apart.

4.3.2. *Skewed flow*

In many practical applications, vortex generators are subject to yaw of the incoming flow. This could be due to either the misalignment of the vortex generators during installation or variations in the flow during operation, such as a vehicle under cornering conditions. This yaw angle leads to an imbalance in the vortex strength in a counter-rotating vortex pair. When investigating the effect of yaw angle, Lögdberg *et al.* (2009) found that increasing the yaw angle in $0 \leq \beta \leq \alpha$ led to a linear increase in the strength of one vortex and a linear decrease in the other, with the total circulation remaining broadly constant. Following this, the relative strengths of the vortices q_1 and q_2 were varied whilst maintaining the total strength $q_1 + q_2$, and it was taken that

$$\frac{q_1 - q_2}{q_1 + q_2} = \frac{\alpha}{\beta}. \tag{4.8}$$

Figure 24(*a*) shows how, by modelling the skew angle in this way, the average circulation over the full domain for the individual vortices follows a linear increase and decrease respectively with the total circulation remaining constant. This matches qualitatively the results of Lögdberg *et al.* (2009).

Figure 24(*b*) displays how the angle of skew affects the total shape factor over the length of the boundary layer (H_{av}). To highlight the change corresponding to the angle, this is shown relative to the shape factor of the case at $\alpha/\beta = 0$ by plotting $H_{av} - H_0^\circ$. As the relative skew angle α/β is increased in the range $0 \leq \alpha/\beta \leq 0.6$, the shape factor stays relatively consistent, with a slight decrease from the level found with 0° of skew. This shows that over this range of skew angles, the effectiveness of the vortex generator to transfer momentum towards the wall and therefore delay the onset of separation is resistant

to skew angle. At skew angles where $0.8 \leq \alpha/\beta \leq 1$, there is an increase in the total shape factor of the downstream boundary layer that would correspond to a reduction in the vortex generator's effectiveness to delay the onset of separation. This step change in the performance of the vortex generator in $0.6 < \alpha/\beta < 0.8$ can also be seen in the coefficients of friction in figures 24(*c*,*d*). Here, two distinct groups can be seen in the behaviour of C_{f_x} and C_{f_z}. For $0 \leq \alpha/\beta \leq 0.6$, higher values of C_{f_x} and C_{f_z} are displayed along the length of the domain, with a drop in both as $\alpha/\beta \geq 0.8$.

5. Conclusions

In this study, we examined a range of cases investigating the effect of the properties of a vortex generator on the development of the streamwise vortices and their subsequent effect on the turbulent boundary layer. Vortex pairs in co-rotating and counter-rotating configurations have been investigated. The efficiency of the numerical method used has allowed for investigations into the effect of both the separation distance of the vortices and the skew angle of the incoming flow, whilst still capturing important turbulence properties accurately.

Initial work looking at an unaffected turbulent boundary layer allowed for the inlet turbulence generation method SEM to be optimised to reduce the development length. It was found that by providing an anisotropic definition of the turbulence length scale at the inlet, the development length was reduced from approximately 15 times the initial boundary layer height to approximately 6 times. By modelling the flow a short distance downstream of a vortex generator by using a pair of Batchelor vortices, the method was validated against previous LES and experimental studies for vortex generators. Both first-order statistics such as the peak streamwise vorticity and the total circulation, and second-order statistics of the turbulence, showed a strong correlation to these previous studies. Having made a direct comparison between the resulting flow developing from the theoretical vortex model and a previous experimental vortex generator flow, the method is applied to further configurations possible as a result of vortex generator design.

By varying the set-up of the Batchelor vortex model at the inlet to the LES domain, comparisons were made between co-rotating and counter-rotating vortex pairs and a single vortex. It was found that over the length of the domain, the counter-rotating pair produced a lower shape factor, thus more momentum is transferred close to the wall, delaying the potential onset of separation. However, it was also noted that as the vortices merge in a co-rotating vortex set-up, the proximity to the wall of one of the vortices, as it is pulled under the other, leads to better momentum transfer in this region, indicated by a lower shape factor. It was also found that by varying the separation distance for co-rotating vortices, the location of the vortices merging could be controlled. This could have the potential to improve the efficiency of the vortex generator if this merging location can be controlled adequately to match the location of the potential separation.

Also investigated was the effect of a skewed inlet flow condition to a vortex generator. This was modelled by an imbalance in the strength of the vortices generated, with the overall strength staying constant. This matched experimental results looking at vortex formation and allowed for the effectiveness of vortex generators in varying skew angle conditions to be assessed. It was found that over a broad range of inlet angles, the effectiveness of the vortices to exchange momentum close to the wall was unaffected, and only at particularly large angles was the effectiveness reduced. Although these variations are not related directly to the specific geometry changes of a vortex generator, they can aid

in practical design decisions through the placement of the generators and through defining an effective operating range.

Funding. This research was funded by a MACE Beacon award. The authors would like to acknowledge the assistance given by Research IT and the use of the Computational Shared Facility at the University of Manchester. The authors would like to thank EPSRC for the computational time made available on the UK supercomputing facility ARCHER and ARCHER2 via the UK Turbulence Consortium (EP/R029326/1).

Declaration of interests. The authors report no conflict of interest.

Author ORCIDs.
Andrew Mole https://orcid.org/0000-0001-9950-0096;
Alex Skillen https://orcid.org/0000-0003-2364-0054;
Alistair Revell https://orcid.org/0000-0001-7435-1506.

Appendix A. IDDES

The WMLES branch of the IDDES model is implemented by providing a rapid switch between a RANS model near the wall and LES away from the wall. This switch is enabled by using a blended length scale definition, L_{WMLES}, common to DES implementations, and given by

$$L_{WMLES} = f_B(1 + f_e)L_{RANS} + (1 - f_B)L_{LES}, \tag{A1}$$

where L_{RANS} and L_{LES} are the RANS and LES length scales, respectively. The function f_B switches smoothly from 1 near the wall to 0 away from the wall, based on the wall distance d_w normalised by the largest cell size h_{max}. It is defined empirically as

$$f_B = \min[2\exp(-9\alpha^2),\ 1.0], \quad \alpha = 0.25 - d_w/h_{max}. \tag{A2a,b}$$

The second empirical function, f_e, is included to alleviate the log-layer mismatch by artificially elevating the RANS Reynolds stresses near the wall. This function combines predefined effects of the wall distance with quantities defined by the flow:

$$f_e = \max[(f_{e1} - 1),\ 1.0]f_{e2}, \tag{A3}$$

$$f_{e1} = \begin{cases} 2\exp(-11.09\alpha^2), & \text{if } \alpha \geq 0, \\ 2\exp(-9.0\alpha^2), & \text{if } \alpha < 0, \end{cases} \quad f_{e2} = 1.0 - \max[f_t, f_l], \tag{A4a,b}$$

$$f_t = \tanh\left[(c_t^2 r_{dt})^3\right], \quad f_l = \tanh\left[(c_l^2 r_{dl})^{10}\right], \tag{A5a,b}$$

where r_{dl} and r_{dt} mark the laminar sublayer and logarithmic parts of the boundary layer, respectively. They are dependent on the solution and are given by

$$r_{dt} = \frac{\nu_t}{\kappa^2 d_w^2 \max\left[\left(\sum_{ij}(\partial \boldsymbol{u}_i/\partial \boldsymbol{x}_j)^2\right)^{1/2},\ 10^{-10}\right]}, \tag{A6}$$

$$r_{dl} = \frac{\nu}{\kappa^2 d_w^2 \max\left[\left(\sum_{ij}(\partial \boldsymbol{u}_i/\partial \boldsymbol{x}_j)^2\right)^{1/2},\ 10^{-10}\right]}. \tag{A7}$$

The constants c_t and c_l are modified for the specific underlying turbulence model used. In the case of the Spalart–Allmaras model used, these are set as $c_t = 1.63$ and $c_l = 3.55$.

References

Aider, J.-L., Beaudoin, J.-F. & Wesfreid, J.E. 2010 Drag and lift reduction of a 3D bluff-body using active vortex generators. *Exp. Fluids* **48** (5), 771–789.

Baker, C.J. 1979 The laminar horseshoe vortex. *J. Fluid Mech.* **95** (2), 347–367.

Baker, C.J. 1980 The turbulent horseshoe vortex. *J. Wind Engng Ind. Aerodyn.* **6** (1–2), 9–23.

Baldacchino, D., Ferreira, C., Ragni, D. & Van Bussel, G.J.W. 2016 Point vortex modelling of the wake dynamics behind asymmetric vortex generator arrays. *J. Phys.: Conf. Ser.* **753** (2), 022025.

Batchelor, G.K. 1964 Axial flow in trailing line vortices. *J. Fluid Mech.* **20** (4), 645–658.

Billard, F., Revell, A. & Craft, T. 2012 Application of recently developed elliptic blending based models to separated flows. *Intl J. Heat Fluid Flow* **35**, 141–151.

Bragg, M.B. & Gregorek, G.M. 1987 Experimental study of airfoil performance with vortex generators. *J. Aircr.* **24** (5), 305–309.

Craft, T.J., Gerasimov, A.V., Launder, B.E. & Robinson, C.M.E. 2006 A computational study of the near-field generation and decay of wingtip vortices. *Intl J. Heat Fluid Flow* **27**, 684–695.

DeGraaff, D.B. & Eaton, J.K. 2000 Reynolds-number scaling of the flat-plate turbulent boundary layer. *J. Fluid Mech.* **422**, 319–346.

Emory, M. & Iaccarino, G. 2014 Visualizing turbulence anisotropy in the spatial domain with componentality contours. In *Center for Turbulence Research Annual Research Briefs*, pp. 123–138.

Esmaili, H. & Piomelli, U. 1992 Temporal development of turbulent boundary layers with embedded streamwise vortices. *Theor. Comput. Fluid Dyn.* **3** (6), 369–380.

Gao, L., Zhang, H., Liu, Y. & Han, S. 2015 Effects of vortex generators on a blunt trailing-edge airfoil for wind turbines. *Renew. Energy* **76**, 303–311.

Godard, G. & Stanislas, M. 2006 Control of a decelerating boundary layer. Part 1: optimization of passive vortex generators. *Aerosp. Sci. Technol.* **10**, 181–191.

Görtler, H. 1955 Strömungslehre. *Z. Angew. Math. Mech.* **35** (9–10), 360–372.

Gritskevich, M.S., Garbaruk, A.V. & Menter, F.R. 2017 A comprehensive study of improved delayed detached eddy simulation with wall functions. *Flow Turbul. Combust.* **98** (2), 461–479.

Guohua, X. & Guanghua, Z. 1998 Longitudinal vortex pair imbedded in a turbulent boundary layer: comparative performances of several turbulence models. *Acta Mech. Sin.* **14** (3), 215–225.

Haase, W., Braza, M. & Revell, A. 2009 *DESider – A European Effort on Hybrid RANS-LES Modelling: Results of the European-Union Funded Project, 2004–2007*, vol. 103. Springer Science & Business Media.

Holgate, J., Skillen, A., Craft, T. & Revell, A. 2019 A review of embedded large eddy simulation for internal flows. *Arch. Comput. Meth. Engng* **26** (4), 865–882.

Jarrin, N., Benhamadouche, S., Laurence, D. & Prosser, R. 2006 A synthetic-eddy-method for generating inflow conditions for large-eddy simulations. *Intl J. Heat Fluid Flow* **27** (4), 585–593.

Kim, W.J. & Patel, V.C. 1994 Influence of streamwise curvature on longitudinal vortices imbedded in turbulent boundary layers. *Comput. Fluids* **23** (5), 647–673.

Laraufie, R. & Deck, S. 2013 Assessment of Reynolds stresses tensor reconstruction methods for synthetic turbulent inflow conditions: application to hybrid RANS/LES methods. *Intl J. Heat Fluid Flow* **42**, 68–78.

Liandrat, J., Aupoix, B. & Cousteix, J. 1987 Calculation of longitudinal vortices imbedded in a turbulent boundary layer. In *Turbulent Shear Flows 5* (ed. F. Durst, B.E. Launder, J.L. Lumley, F.W. Schmidt & J.H. Whitelaw), pp. 253–265. Springer.

Liu, J., Piomelli, U. & Spalart, P.R. 1996 Interaction between a spatially growing turbulent boundary layer and embedded streamwise vortices. *J. Fluid Mech.* **326**, 151–179.

Lögdberg, O., Fransson, J.H.M. & Alfredsson, P.H. 2009 Streamwise evolution of longitudinal vortices in a turbulent boundary layer. *J. Fluid Mech.* **623**, 27–58.

Mehta, R.D. & Bradshaw, P. 1988 Longitudinal vortices imbedded in turbulent boundary layers. Part 2. Vortex pair with 'common flow' upwards. *J. Fluid Mech.* **188**, 529–546.

Mockett, C., Haase, W. & Schwamborn, D. (Ed.) 2017 *Go4Hybrid: Grey Area Mitigation for Hybrid RANS-LES Methods*. Springer.

Osterlund, J., Lindgren, B. & Johansson, A. 2003 Flow structures in zero pressure-gradient turbulent boundary layers at high Reynolds numbers. *Eur. J. Mech. B/Fluids* **22**, 379–390.

Pauley, W.R. & Eaton, J.K. 1988 Experimental study of the development of longitudinal vortex pairs embedded in a turbulent boundary layer. *AIAA J.* **26** (7), 816–823.

Pearcy, H.H. 1961 *Boundary Layer and Flow Control: Its Principle and Applications*, 2nd edn. Elsevier Ltd.

Pegrum, J.M. 2007 Experimental study of the vortex system generated by a Formula 1 front wing. PhD thesis, Imperial College London.

Piomelli, U. 2008 Wall-layer models for large-eddy simulations. *Prog. Aerosp. Sci.* **44** (6), 437–446.

RUMSEY, C., SMITH, B. & HUANG, G. 2009 Description of a website resource for turbulence modeling verification and validation. https://doi.org/10.2514/6.2010-4742.

SANKARAN, L. & RUSSELL, D.A. 1990 A numerical study of longitudinal vortex interaction with a boundary layer. In *21st Fluid Dynamics, Plasma Dynamics and Lasers Conference*. *AIAA Paper* 1990-1630.

SCHLATTER, P. & ÖRLÜ, R. 2010 Assessment of direct numerical simulation data of turbulent boundary layers. *J. Fluid Mech.* **659**, 116–126.

SHUR, M.L., SPALART, P.R., STRELETS, M.K. & TRAVIN, A.K. 2008 A hybrid RANS-LES approach with delayed-DES and wall-modelled LES capabilities. *Intl J. Heat Fluid Flow* **29** (6), 1638–1649.

SKILLEN, A., REVELL, A. & CRAFT, T. 2016 Accuracy and efficiency improvements in synthetic eddy methods. *Intl J. Heat Fluid Flow* **62**, 386–394.

SPALART, P. & ALLMARAS, S. 1992 A one-equation turbulence model for aerodynamic flows. In *30th Aerospace Sciences Meeting and Exhibit*. *AIAA Paper* 1992-439.

SPALART, P.R. & RUMSEY, C.L. 2007 Effective inflow conditions for turbulence models in aerodynamic calculations. *AIAA J.* **45** (10), 2544–2553.

SPALART, P.R., SHUR, M.L., STRELETS, M.K. & TRAVIN, A.K. 2015 Direct simulation and RANS modelling of a vortex generator flow. *Flow Turbul. Combust.* **95** (2–3), 335–350.

SPALART, P.R. & WATMUFF, J.H. 1993 Experimental and numerical study of a turbulent boundary layer with pressure gradients. *J. Fluid Mech.* **249**, 337–371.

SPANGENBERG, W.G. & SCHUBAUERAND, G.B. 1960 Forced mixing in boundary layers. *J. Fluid Mech.* **8** (1), 10–32.

TAYLOR, H.D. 1947 The elimination of diffuser separation by vortex generators. *Tech. Rep.* United Aircraft Corporation.

TORII, K. & YANAGIHARA, J.I. 1997 A review on heat transfer enhancement by longitudinal vortices. *J. Heat Transfer Soc. Japan* **36** (142), 73–86.

VELTE, C.M., HANSEN, M.O.L. & OKULOV, V.L. 2009 Helical structure of longitudinal vortices embedded in turbulent wall-bounded flow. *J. Fluid Mech.* **619**, 167–177.

WELLER, H.G., TABOR, G., JASAK, H. & FUREBY, C. 1999 A tensorial approach to computational continuum mechanics using object-oriented techniques. *Comput. Phys.* **12** (6), 620–631.

WENDT, B.J. 2001 Initial circulation and peak vorticity behavior of vortices shed from airfoil vortex generators. NASA/CR–2001-211144.

WESTPHAL, R.V., PAULEY, W.R. & EATON, J.K. 1987 Interaction Between a Vortex and a Turbulent Boundary Layer Part I: Mean Flow Evolution and Turbulence Properties. NASA Tech Rep. TM 88361.